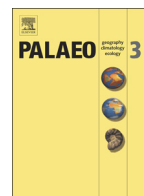




Contents lists available at ScienceDirect

## Palaeogeography, Palaeoclimatology, Palaeoecology

journal homepage: [www.elsevier.com/locate/palaeo](http://www.elsevier.com/locate/palaeo)

## Regional depositional changes and their controls on carbon and sulfur cycling across the Ordovician–Silurian boundary, northwestern Guizhou, South China

Yifan Li <sup>a,b,\*</sup>, Juergen Schieber <sup>c</sup>, Tailiang Fan <sup>a,b</sup>, Zhiyang Li <sup>c</sup>, Junpeng Zhang <sup>d,\*\*</sup>

<sup>a</sup> School of Energy Resources, China University of Geosciences (Beijing), Beijing 100083, China

<sup>b</sup> Key Laboratory of Marine Reservoir Evolution and Hydrocarbon Accumulation Mechanism, Ministry of Education, China University of Geosciences (Beijing), Beijing 100083, China

<sup>c</sup> Department of Geological Sciences, Indiana University, Bloomington, IN 47403, United States

<sup>d</sup> Nanjing Institute of Geology and Palaeontology, Chinese Academy of Sciences, Nanjing 210008, China

## ARTICLE INFO

## Article history:

Received 18 April 2017

Received in revised form 29 July 2017

Accepted 31 July 2017

Available online xxxxx

## Keywords:

Yangtze Platform

Hirnantian event

Wufeng–Longmaxi succession

Black shales

Stable isotopic geochemistry

## ABSTRACT

The controls of regional depositional environment on stable isotope records spanning the Ordovician–Silurian boundary on the Yangtze Platform have seldom been investigated. The objectives of this study include reconstruction of regional depositional settings and assessment of how sedimentary processes may have influenced carbon- and sulfur-isotopic fractionation. Seven shale facies have been recognized in the Wufeng–Longmaxi interval from two locations. Completely bioturbated claystone of the basal Wufeng Formation accumulated on a shallow oxygenated muddy shelf. Overlying faintly banded black siliceous shale suggests deposition under deep anoxic conditions interrupted by episodes of dysoxia. Muddy fossiliferous facies of the Guanyinqiao Formation reflects a glacial sea-level lowstand setting, and the observed proximal to distal heterogeneity of facies matrix supports shallowing in the proximal area. Overlying faintly banded black shale of the Longmaxi Formation tells of a post-glacial transgression. The carbonaceous deposits are overlain by banded gray and dark gray muddy siltstones and suggest a shoaling upward trend. The shallow-water facies display relatively heavier  $\delta^{13}\text{C}_{\text{org}}$  values, whereas deep-water facies are characterized by lower  $\delta^{13}\text{C}_{\text{org}}$  values. Discrepancies between Hirnantian positive  $\delta^{13}\text{C}_{\text{org}}$  excursions in proximal and distal areas probably reflect spatial gradient in seawater  $\delta^{13}\text{C}_{\text{DIC}}$  induced by glacioeustasy. Deposits accumulated under oxic and physically dynamic conditions display strong positive  $\delta^{34}\text{S}_{\text{sulfide}}$  excursions, perhaps a consequence of diagenetic sulfate reduction occurred at some depth below the sediment–water interface and removed from the sulfate pool of overlying water column. Negative relationship between  $\delta^{34}\text{S}_{\text{sulfide}}$  and TOC indicates that redox conditions and physical reworking of sediment at the sediment–water interface controlled the rate of microbial sulfate reduction and sulfur isotope fractionation. Overall, co-variation of lithofacies and isotopic records suggests that local heterogeneity of seawater chemistry and sedimentary dynamics may exert partial controls on biogeochemical processes and amplify the magnitude of the Hirnantian isotopic excursions in the proximal area.

© 2017 Elsevier B.V. All rights reserved.

## 1. Introduction

The Ordovician–Silurian (O–S) transition is a critical time period of Earth's history because of a coincidence between glaciation events, mass extinctions and tectonic activity (Algeo et al., 2016). Recently, the Ordovician–Silurian fine-grained sedimentary succession of the Yangtze Platform have been investigated more closely because it preserves the record of biogeochemical processes at this time period (e.g. Fan et al., 2009; Li et al., 2015a; Wang et al., 1997; Yan et al., 2010, 2012, 2009; Zhang et al., 2000). High-resolution carbon and sulfur

isotope chemostratigraphic data spanning the O–S boundary in several outcrop sections on the Yangtze Platform have been related to global climate change and glacial events (e.g. Fan et al., 2009; Gorjan et al., 2012; Yan et al., 2009; Zhang et al., 2009). However, data collected elsewhere in the world (LaPorte et al., 2009; Melchin and Holmden, 2006; Melchin et al., 2013) suggest that C- and S-cycling processes reflected in isotope records can be affected by regional variations of depositional environment. Although extensive sedimentologic and sequence stratigraphic studies have been conducted in the past decade (e.g. Chen et al., 2004; Li et al., 2012; Liang et al., 2012; Zheng et al., 2013), few have focused on how sedimentary processes influence carbon and sulfur cycling in the ocean. Recent examination of other black shale successions indicates that these deposits are typically heterogeneous at different scales and can be differentiated into suites of microfacies that reflect different

\* Correspondence to: Y. Li, School of Energy Resources, China University of Geosciences (Beijing), Beijing 100083, China.

\*\* Corresponding author.  
E-mail address: [liyifan@cugb.edu.cn](mailto:liyifan@cugb.edu.cn) (Y. Li).

sedimentary processes (e.g. Bohacs, 2005; Bohacs et al., 2014; Lazar, 2007; Macquaker et al., 2010, 2007; Schieber, 1990, 1994, 1999, 2011b; Schieber and Lazar, 2004; Schieber et al., 2010). Therefore, it is necessary to examine the Wufeng-Longmaxi interval in terms of sedimentary processes and facies characteristics as a means of assessing the degree to which these factors impact C- and S-cycling. To this end, we provide a detailed description (texture, composition, and sedimentary structure) and facies analysis via petrographic examination, optical microscopy, SEM, and geochemical analysis, from two drill cores in northwestern Guizhou Province, in order to evaluate the influence of regional depositional controls on C- and S-cycling processes.

## 2. Geological setting

The South China Block comprises two sub-blocks, the Yangtze and Cathaysia blocks, that amalgamated along the Jiangnan suture in the Proterozoic around 860 Ma (Wang et al., 2012; Yao et al., 2013). It became attached to Gondwana by Late Ordovician to Early Silurian time

during the Wuyi-Yunkai orogeny (Fig. 1) (Metcalfe, 1994, 2013). This event was accompanied by deformation and metamorphism over much of southeastern South China, and the development of a foreland basin on the northwestern Cathaysia Block and southern Yangtze Block (Li et al., 2010; Metcalfe, 1994, 2013; Su et al., 2009). Meanwhile, the territory of the Yangtze basin concentrated in the south and west as a consequence of thrust-related uplift (Songpan and Dian-Qian) (Golonka, 2009, 2012; Golonka et al., 2006). The Yangtze Sea is a part of the South China Block and regarded as a silled epicontinental sea (Fig. 1B) (Chen et al., 2004, 1987; Golonka, 2009, 2012; Golonka et al., 2006; Rong and Chen, 1987). The fine-grained Ordovician-Silurian succession (up to 522 m thick) (Fig. 2), including the Wufeng, Guanyinqiao, and Longmaxi formations, is present from the Sichuan to the Guizhou province. These deposits are considered to record a history of regression and transgression caused by migration of the foreland basin and forebulge (Su et al., 2009) and glacial advance and retreat (Melchin et al., 2013; Mitchell et al., 2011; Moreau, 2011; Schönlaub et al., 2011).

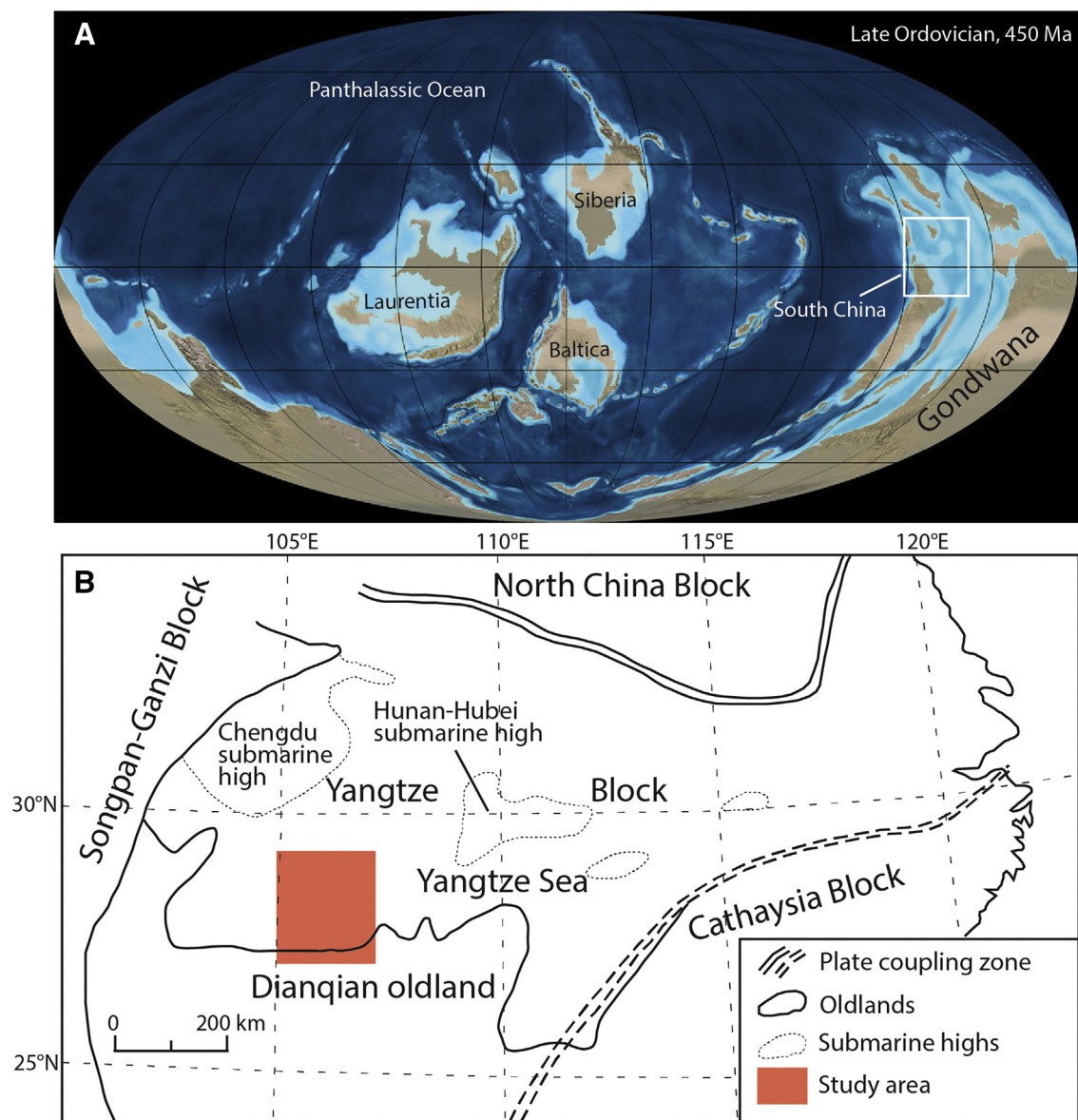


**Fig. 1.** (A) Late Ordovician paleogeographic map (450 Ma) showing location of South China (white rectangle). Various paleocontinents and paleocean are indicated. Base map is courtesy of R.C. Blakey (<http://www.cpgeosystems.com/globaltext2.html>). (B) Paleogeographic map (Katian age) of South China Block. Location of study area is indicated by light red filled rectangle. The term “oldland” is equivalent to ancient continent. (For interpretation of the references to color in this figure legend, the reader is referred to the web version of this article.) Modified from Chen et al. (2004) and Yan et al. (2012).

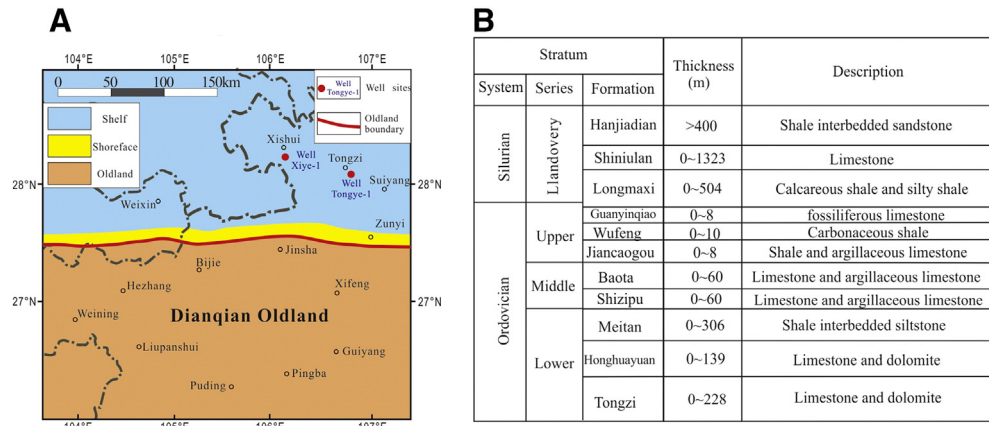


Fig. 2. (A) Location of the studied well cores. (B) Stratigraphic column of the Ordovician and Silurian in northwestern Guizhou area. The term “oldland” is equivalent to ancient continent.

Two well cores, Tongye-1 and Xiye-1, in northwestern Guizhou area were examined. According to recent research on paleotopography (Chen et al., 2017; Zhang et al., 2014; 2016), Tongye-1 well is located in the proximal area (~5 km east of Tongzi County), whereas Xiye-1 well is located in the distal area (~20 km south from Xishui County) (Fig. 2A). Both wells contain the Wufeng, Guanyinqiao, and Longmaxi formations (Fig. 3). The Wufeng Formation, dominated by graptolite-bearing shale, is mainly of Katian and earliest Hirnantian age (Fig. 3), resulting from a transgression induced by the Boda warming event (e.g. Armstrong et al., 2009; Brenchley and Storch, 1989; Fortey and Cocks, 2005). Graptolite biozonation ranges from the *D. complexus* to

the *P. pacificus* Zone (Fig. 4) (Rong et al., 2011, 2010). The overlying Guanyinqiao Formation (Fig. 3), characterized by beds of shelly fauna, occupies the age range of the *N. extraordinarius* and *N. persculptus* Zone (Fig. 4) (Rong et al., 2011, 2010). The graptolite-rich Longmaxi Formation is much thicker than the prior two units (Fig. 3). The lower Longmaxi section is of Rhuddanian age, and in the distal area ranges from the *A. ascensus* to *P. cyphus* graptolite Zones (Fig. 4) (Rong et al., 2011). In the proximal area, however, the basal *A. ascensus* and *P. acuminatus* Zones are missing, and the Longmaxi Formation is paraconformably overlies the Guanyinqiao Formation (Fig. 4) (Rong et al., 2011).

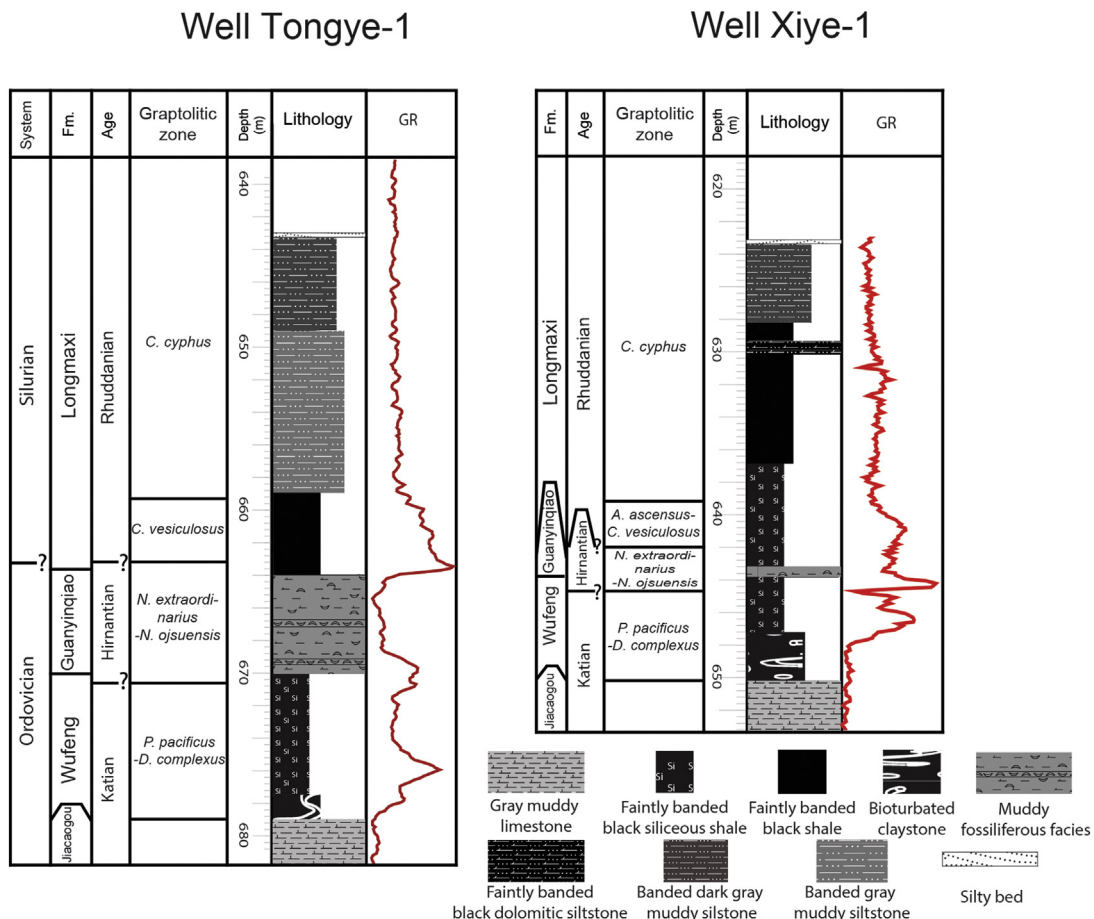


Fig. 3. Lithostratigraphy of the Wufeng-Longmaxi succession of the Tongye-1 and well Xiye-1 cores.

Strata		Graptolite zone	Xishui	Tongzi		
System	Age		Donghuang	Daijiagou	Shanwangmiao	Sancha
Silurian	Rhuddanian	<i>Coronograptus cyphus</i>	Longmaxi	Longmaxi	Longmaxi	Longmaxi
		<i>Cystograptus vesiculosus</i>				
		<i>Parakidograptus acuminatus</i>				
		<i>Akidograptus ascensus</i>				
Ordovician	Hirnantian	<i>Nomalograptus persculptus</i>	Guanyinqiao	Guanyinqiao	Guanyinqiao	Guanyinqiao
		<i>Nomalograptus extraordinarius</i>				
	Katian	<i>D. mirus</i>	Wufeng	Wufeng	Wufeng	Wufeng
		<i>P. sinensis</i>				
		<i>D. complexus</i>				

Fig. 4. Graptolite zones spanning the Ordovician–Silurian boundary and their stratigraphic correlations in Xishui and Tongzi area. Modified from Rong et al. (2011).

3. Materials and methods

Cores recovered from the Tongye-1 and Xiye-1 wells were described at decimeter scale. Thirty five samples of different lithofacies were cut and polished for detailed examination. Thirty seven thin sections were examined under the optical microscope (transmitted and reflected light). Twenty seven chip samples were prepared by edge milling with a GATAN Iliion ion mill for high resolution scanning electron microscope (SEM) imaging (secondary electrons (SE), backscattered electrons (BSE), and cathodoluminescence (CL) imaging). Thirty five samples of different lithofacies were selected for analysis of total organic carbon content (TOC),  $\delta^{13}C_{org}$  and  $\delta^{34}S_{sulfide}$  values (Table 1). These samples were milled into homogeneous powders. Sedimentary sulfide was extracted from powdered samples (~1 g) for  $\delta^{34}S_{sulfide}$  analysis by wet chemical extraction and trapped as Ag<sub>2</sub>S in a modified procedure described in previous studies (Brüchert, 1998; Lefticariu et al., 2006). Sample powders (~1 g) for  $\delta^{13}C_{org}$  analysis were dissolved with 6-N HCl to remove carbonate minerals. Decalcified residues were repeatedly rinsed in deionized water, centrifuged, and oven-dried overnight (80 °C). The dried samples were homogenized, weighed, and loaded into tin cups for  $\delta^{13}C_{org}$  analysis. The  $\delta^{34}S_{sulfide}$  and  $\delta^{13}C_{org}$  were measured via SO<sub>2</sub> and CO<sub>2</sub> generated by a Costech elemental analyzer (EC4010) coupled with a Thermo Finnigan Delta V Plus mass spectrometer in continuous flow mode at the Indiana University Bloomington Stable Isotope Research Facility (SIRF). Values are expressed using  $\delta$  notation and reported in per mille (‰), where,

$$\delta X = [(R_{sample}/R_{standard}) - 1] \times 10^3 \quad (1)$$

$$X = {}^{13}C \text{ or } {}^{34}S \text{ and } R = {}^{13}C/{}^{12}C \text{ or } {}^{34}S/{}^{32}S \quad (2)$$

S-isotope values are reported relative to Vienna Cañon Diablo Troilite (VCDT) for sulfur. Internal laboratory standards ERE and EMR were used as reference standards with values of -4.7‰ and +0.9‰,

Table 1  
Geochemical results of samples from Ordovician–Silurian succession at well Tongye-1 and well Xiye-1, northwestern Guizhou.

Samples	Depth (m)	Lithofacies	TOC (%)	$\delta^{13}C_{org}$ (‰)	$\delta^{34}S_{sulfide}$ (‰)
Well Tongye-1					
TY-5	656.35	Banded gray muddy siltstone	0.50	-29.25	-14.56
TY-4	659.8	Faintly banded black shale	5.27	-30.34	-0.55
TY-3	661.3	Faintly banded black shale	5.11	-29.71	-0.21
TY-2	663.06	Faintly banded black shale	9.10	-29.98	13.51
TY-1	665.2	Muddy fossiliferous facies	0.93	-28.75	12.63
TY-1T	666.6	Muddy fossiliferous facies	0.96	-28.75	14.74
TY-2T	667.3	Muddy fossiliferous facies	0.66	-28.32	15.03
TY-3T	669	Muddy fossiliferous facies	3.75	-28.96	0.97
TY-4T	670.5	Faintly banded black siliceous shale	4.17	-30.30	-7.01
TY-5T	672.75	Faintly banded black siliceous shale	4.38	-30.47	-20.12
TY-6T	674.65	Faintly banded black siliceous shale	5.46	-30.65	-25.84
TY-7T	675.2	Faintly banded black siliceous shale	4.89	-30.85	-22.49
TY-8T	676.15	Faintly banded black siliceous shale	6.61	-30.53	-28.77
TY-9T	678.2	Bioturbated claystone	5.07	-30.37	-12.99
Well Xiye-1					
XY-15	623.3	Banded dark gray muddy siltstone	1.23	-29.75	-7.19
XY-14	624.75	Banded dark gray muddy siltstone	0.96	-29.81	-6.67
XY-11	629.2	Faintly banded black shale	2.88	-30.80	-1.69
XY-13	629.4	Faintly banded black dolomitic siltstone	4.10	-21.18	-6.16
XY-12	630.3	Faintly banded black shale	3.02	-30.52	3.42
XY-10	636.9	Faintly banded black siliceous shale	2.69	-30.75	1.05
XY-7	637.3	Faintly banded black siliceous shale	2.84	-30.79	-4.98
XY-9	637.7	Faintly banded black siliceous shale	3.67	-30.81	-3.91
XY-8	638.7	Faintly banded black siliceous shale	3.29	-30.95	-6.45
XY-6	641.95	Faintly banded black siliceous shale	4.11	-30.96	-1.17
XY-5	643.7	Muddy fossiliferous facies	3.51	-30.28	5.74
XY-4	644.2	Faintly banded black siliceous shale	5.77	-30.98	-19.06
XY-3	647.3	Bioturbated claystone	1.30	-30.51	21.75
XY-2	649.5	Bioturbated claystone	1.15	-29.55	10.76

respectively. C-isotopic values were calibrated against the international standards EDTA-1 (-40.45‰) and Acetanilide B (-29.52‰), and are reported relative to Vienna Peedee Belemnite standard (VPDB). The precisions for  $\delta^{34}S_{sulfide}$  and  $\delta^{13}C_{org}$  are ±0.3‰ and ±0.2‰, respectively.

4. Results

4.1. Lithofacies

Seven shale facies were identified in these two sections based on texture (grain size), bedding, composition and bioturbation index (Fig. 3). The degree of bioturbation varies from no visible burrows to no remnant bedding when a rock interval is fully homogenized, and can be assessed using 0- to 5-scale (Taylor and Goldring, 1993; Lazar et al., 2015). Stratigraphic distributions of these facies as follows (Fig. 3): (1) bioturbated claystone are recognized in the basal Wufeng Formation; (2) faintly banded black siliceous shales comprise the bulk of the Wufeng Formation as well as the basal Longmaxi Formation of well Xiye-1; (3) faintly banded black shale is present in the lower part of the Longmaxi Formation; (4) muddy fossiliferous facies is observed in the Guanyinqiao Formation of both sections though much thicker in

the Tongye-1 well; (5) faintly banded black dolomitic siltstone is identified only in the Longmaxi Formation of the Xiye-1 well where it is interbedded with faintly banded black shale; (6) banded gray muddy siltstone is recognized only in the Longmaxi Formation of the Tongye-1 well; and (7) banded dark gray muddy siltstone is present in the Longmaxi Formation. Shale and mudstone are both widely used terms for fine-grained sedimentary deposits. However, because of the historical use of the term “shale” in the stratigraphic designation (Wufeng and Longmaxi shales), and also for simplicity, we will primarily use the term

shale in this contribution, with the understanding that it includes what some prefer to identify as mudstones.

#### 4.1.1. Bioturbated claystone

This lithofacies, observed in 3 samples from the basal Wufeng Formation of both sections (Fig. 3), contains about 50% clay minerals, 30% quartz, and 10% carbonate. It overlies gray muddy limestone of the Jiancaogou Formation (Fig. 3). The dominant grain size is <8  $\mu$ m. Bioturbated claystone typically forms stacked successions

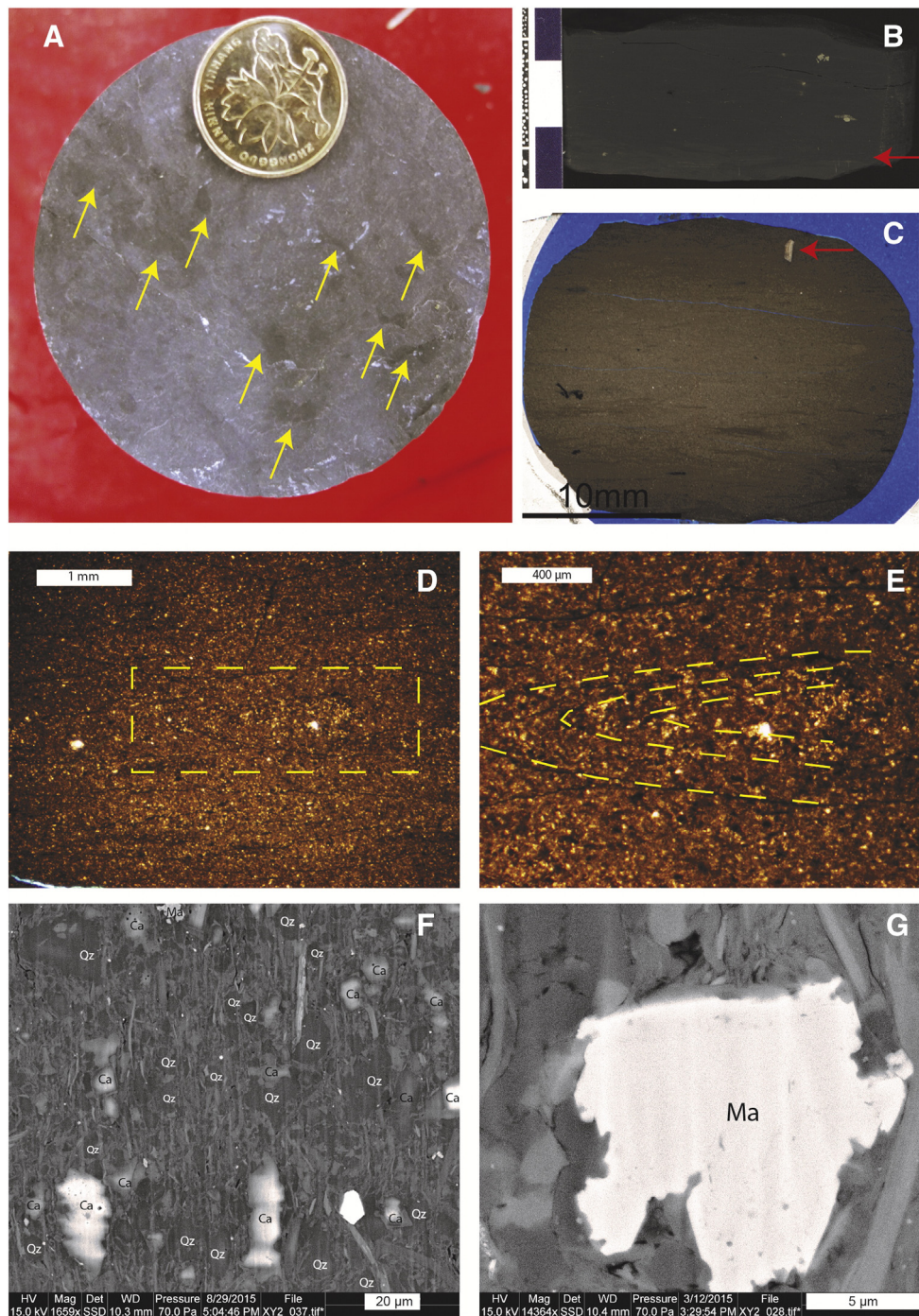


**Fig. 5.** Sedimentary features of the bioturbated claystone. (A) Transverse view of core sample XY-2 (646.6 m). Yellow arrows point to dark gray bioturbation. (B) Longitudinal view of core sample XY-2. A red arrow indicates a boundary between dark gray bioturbated layer and black bioturbated layer. (C) Photomicrograph of XY-2 (thin section). A red arrow points to a fossil fragment. Notice the completely bioturbated nature of the sample. (D) Zoophycos found in the XY-2. (E) Close-up image of Zoophycos (outlined by dashed yellow line). (F) BSE image of the bioturbated claystone (XY-2) showing widespread detrital quartz grains. The SEM sample was viewed on surface oriented perpendicular to bedding. (G) BSE image of marcasite found in XY-2. Qz = quartz, Ca = Calcite, Ma = marcasite. (For interpretation of the references to color in this figure legend, the reader is referred to the web version of this article.)

(average thickness = 1.5 m) of interbedded dark gray bioturbated claystone and black bioturbated claystone (Fig. 5A, B). These deposits are fully homogenized by bioturbation (e.g. *Zoophycos* isp.) (Bioturbation index = 5; Taylor and Goldring, 1993; Lazar et al., 2015) (Fig. 5B–E). Sparse shelly fragments are observed locally (Fig. 5C). Most quartz grains are detrital in origin (tested by CL; Schieber et al., 2000; Zinkernagel, 1978) (Fig. 5F). Sulfide minerals, dominantly marcasite (spearhead shapes and well developed cleavage) (Fig. 5G) in addition to pyrite, are disseminated throughout the matrix. Bioturbated claystone of the Tongye-1 core is more organic matter (TOC as much as 5.07%) than equivalent deposits of the Xiye-1 core (TOC = 1.15–1.30%).

#### 4.1.2. Faintly banded black siliceous shale

The faintly banded black siliceous shale facies is characterized by high quartz contents (>50%), ranging from 50 to 70%. The clay mineral content is relatively low, ranging from 12 to 27%. Grain size ranges from 8  $\mu\text{m}$  to 32  $\mu\text{m}$ . Deposits of this facies are commonly organized as stacked successions of faint thin bands, some of which are marked by

continuous or discontinuous silty laminae (Fig. 6A, B). Flattened silt/clay peloids (Fig. 6C, D) as well as radiolaria are common to this facies (Fig. 6D). Most quartz grains display dull red CL color, gray blue CL color or non-luminescent color (Fig. 6E, F, dwell time is 1000  $\mu\text{s}$  per pixel). According to classification of the CL color of quartz (Götze and Zimmerle, 2000), quartz grains with no CL or weakly luminescent color are authigenic origin. Thus, most quartz grains in this facies are authigenic. However, detrital quartz grains become more abundant upward through this facies in the Tongye-1 core, whereas the proportion of authigenic quartz remains constant in the Xiye-1 core. Carbonate grains, mostly as calcite cement, are distributed throughout the matrix of these deposits. Pyrite framboids are common within the matrix (Fig. 6E).

#### 4.1.3. Muddy fossiliferous facies

This facies, enriched in shelly fossils debris, is characterized by interspersed fossil-rich layers. It is commonly organized into stacked successions of interbedded fossil-rich layers and background rock containing sparse fossils. The composition of the background matrix varies

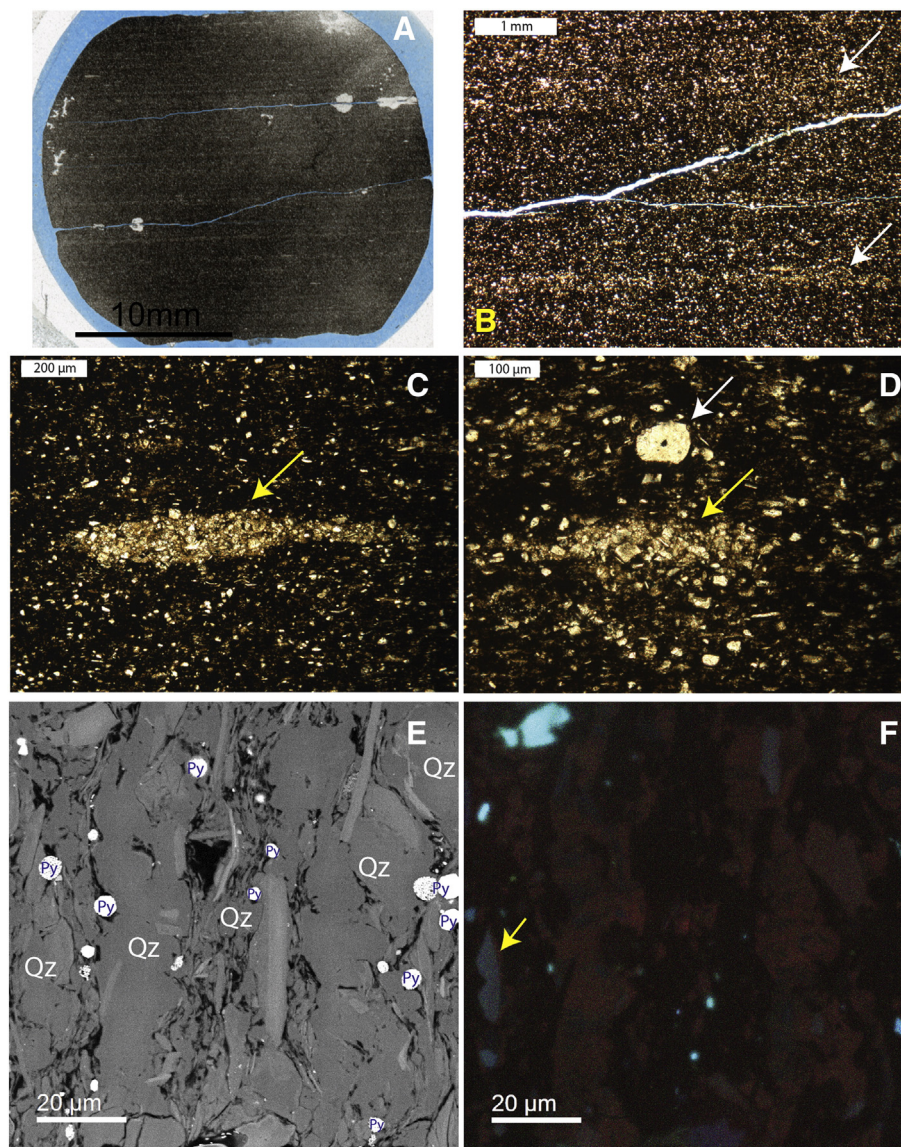


**Fig. 6.** Sedimentary features of the faintly banded black siliceous shale. (A) Photomicrograph of XY-8 (638.7 m). Notice faint bands and parallel discontinuous laminae. (B) Close-up of faint bands (indicated by white arrows). (C) A flattened fecal pellet (yellow arrow) observed in sample XY-8. (D) A flattened fecal pellet (yellow arrow) and a radiolarian (white arrow) found in sample XY-8. (E) BSE image of siliceous shale (TY-8T) showing widespread disseminated framboid pyrite. (F) CL image of siliceous shale (TY-8T). Dull red CL and gray blue CL inside it indicate diagenetic silica and early diagenetic silica, respectively. Light blue CL in the left center (yellow arrow) indicates detrital silica (quartz). All SEM samples were viewed on surfaces oriented perpendicular to bedding. Qz = quartz. (For interpretation of the references to color in this figure legend, the reader is referred to the web version of this article.)

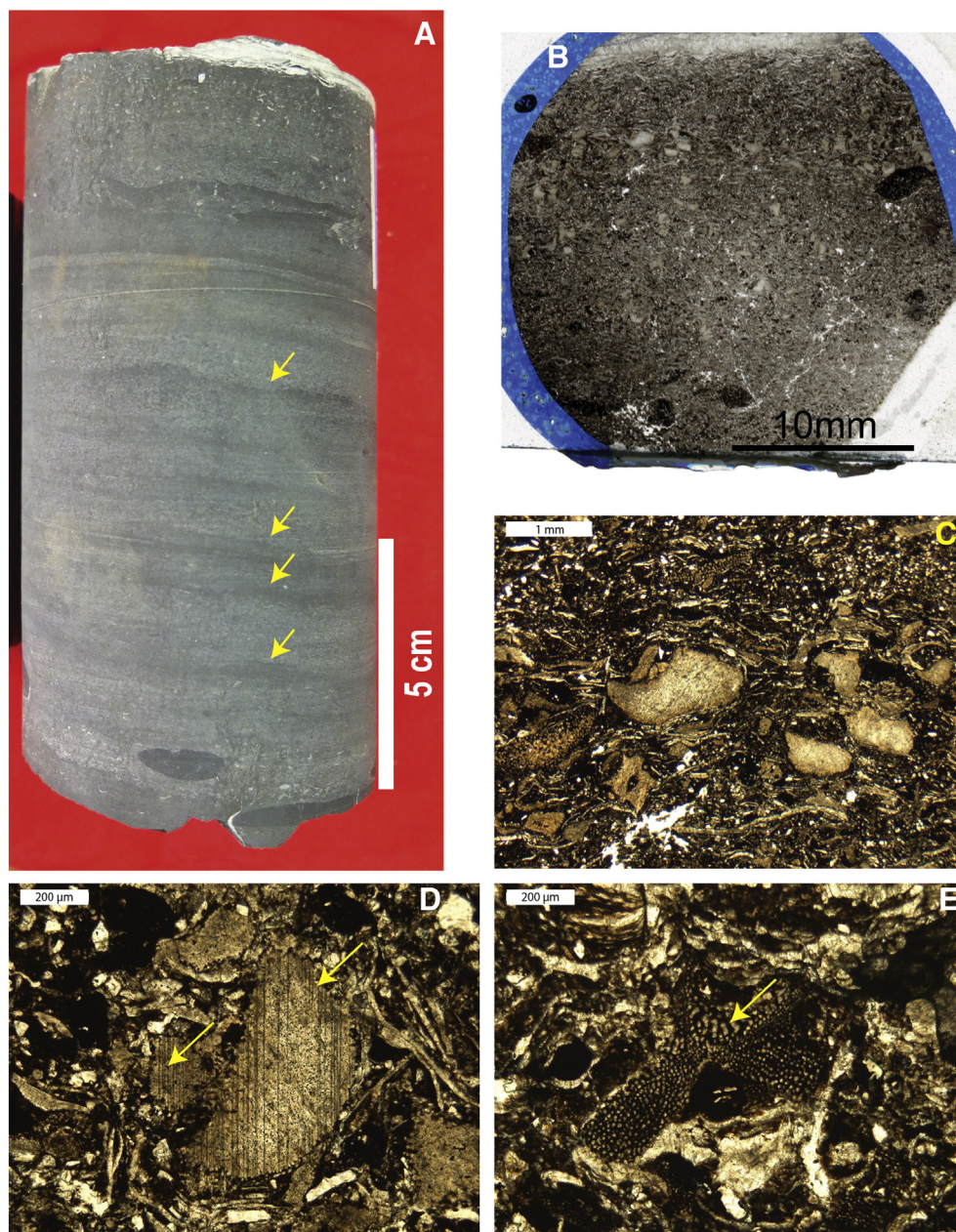


**Fig. 7.** Sedimentary features of a muddy fossiliferous facies sample (TY-3T, 669 m) of the Tongye-1 core. The background matrix is siltstone. (A) Longitudinal view of core sample TY-3T. Yellow arrows indicate wavy beds. (B) Photomicrograph of a fossil-rich layer in sample TY-3T. Note widespread of fossil fragments. (C) Close-up image of the fossil-rich layer. Notice the background matrix is siltstone. (D) Crinoid fragments (yellow arrows) found in sample TY-3T. (E) A fragment of bryozoan (yellow arrow). (For interpretation of the references to color in this figure legend, the reader is referred to the web version of this article.)

markedly in stratigraphic profile; quartz ranges from 6.5 to 57.6%; carbonate ranges from 16.8 to 84.6%; and clay minerals vary from 7.2 to 27.4%. Background matrix of the Tongye-1 core displays an upward progression from siltstone, including wavy beds (Fig. 7A), to bioturbated micrite (Fig. S1A–D), and micrite (Fig. S2E, F). This facies is much thinner in the Xiye-1 core (Fig. 3) and just has siliceous shale as its background matrix (Fig. 8A, B). The background matrix has diagenetic silica and calcite mixed in with clay mineral (Fig. 8C, D). Diverse shelly fossils were identified in these deposits, including brachiopods, bryozoans, crinoids, sponge spicules, ostracods, trilobites, and foraminifera (Figs. 7D, E, 8B, S1F). Large pieces (1–2 mm) of fragile fossil shells, for example, brachiopods are preserved (Fig. 8B). The orientation of shelly fossils appears random (Fig. 8C, A). Disseminated grains of pyrite and euhedral marcasite are a common constituent of these deposits (Fig. S1C).

Diagenetic phosphate and phosphatic pellets are also preserved within the matrix (Fig. S1D).

#### 4.1.4. Faintly banded black shale

Deposits of this facies are characterized by less quartz (33–45%) and more abundant clay minerals (30–40%) than those of the faintly banded black siliceous shale. Average particle size ranges from 8  $\mu\text{m}$  to 32  $\mu\text{m}$ . This facies typically consists of faintly banded organic-rich shale contains parallel, discontinuous silt laminae (Fig. S2A). Although authigenic silica is present in the shale matrix, detrital quartz grains dominate the quartz population (tested by CL, Schieber et al., 2000; Zinkernagel, 1978) (Fig. S2B). Black shale associated with occasional bentonite layers contains parallel laminae enriched in pyrite. The basal portion of this facies in the Tongye-1 core contains higher carbonate contents than the

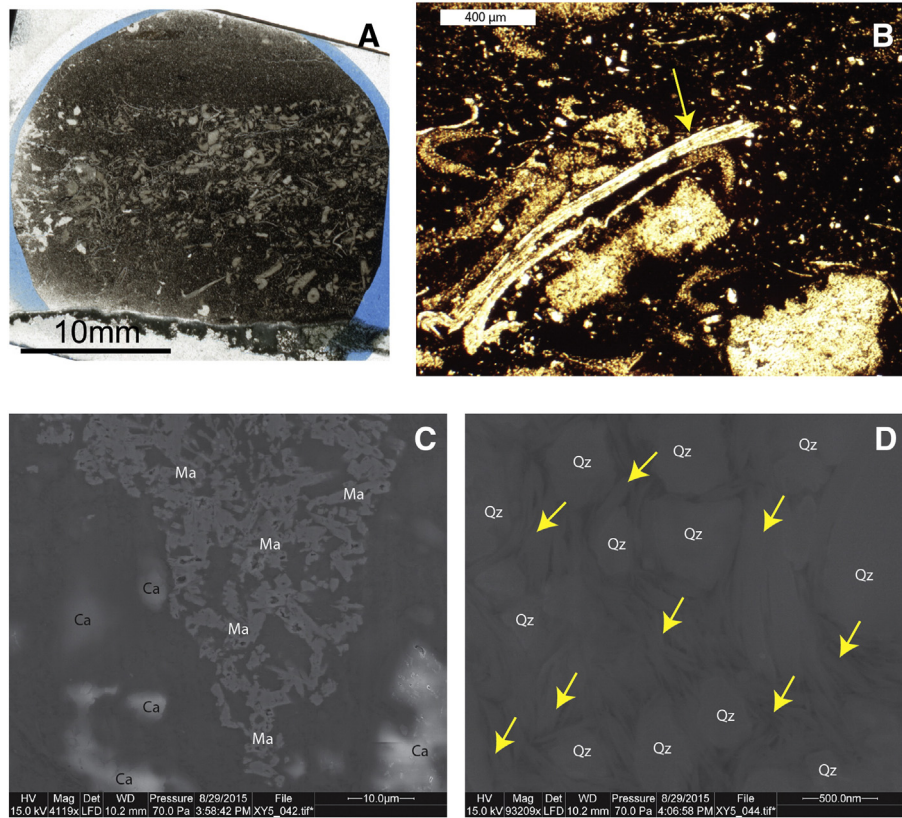


**Fig. 8.** (A) Photomicrograph of a muddy fossiliferous facies sample (XY-5, 643.7 m) of the Xiye-1 core. The background matrix is siliceous shale. (B) A fragile piece of brachiopod (yellow arrow) in sample XY-5. (C) SE image of XY-5 (643.7 m). Notice disseminated diagenetic calcite cements. (D) Close-up SE image of the background matrix showing diagenetic silica mixed with clay minerals. All SEM samples were viewed on surfaces oriented perpendicular to bedding. Ca = Calcite, Ma = Marcasite, Qz = quartz. (For interpretation of the references to color in this figure legend, the reader is referred to the web version of this article.)

upper portion of this facies (Fig. S2B). Diagenetic phosphate was also found within the matrix of the basal Longmaxi Formation (Fig. S2C, D).

#### 4.1.5. Faintly banded black dolomitic siltstone

This facies, interspersed within faintly banded black shale, contains abundant dolomite (as much as 62.5%) and is observed only in the Xiye-1 core (Fig. 3). Faintly banded black dolomitic siltstone typically consists of intercalated faint dolomitic bands and discontinuous silty laminae (Fig. S3A, B). Dolomite grains are generally between 30 µm and 50 µm in size (Fig. S3C, D). Disseminated pyrite framboids are common to this facies (Fig. S3D).

#### 4.1.6. Banded gray muddy siltstone

This facies is observed only in the Tongye-1 core (Fig. 3). Analyzed samples contain 35–40% quartz and 31–35% clay minerals. Most quartz grains are silt size and of detrital origin. The lower interval of this facies comprises intercalated sharply bounded thick silt bands (up to 8 mm), bundles of silt laminae, and clay-rich layers (Fig. S4A–C). Banding appears to reflect rapid deposition of fine-grained clastics with distinct compositional attributes, organic content, grain size variation, and horizontal cryptobioturbation (Wilson, 2012). Unlike laminae, bands are usually characterized by diffuse boundaries. Some silt-rich laminae are wavy and/or lenticular (Fig. S4A). Coarser silts tend to accumulate in silt laminae and bands, whereas finer silt is dispersed among clays (Fig. S4C). The upper part of this facies is characterized by thinner silty bands (Fig. 9A, B). Burrows can be observed in clay-rich layers (Fig. 9C, D). Most silty bands are cemented by calcite and appear to have been disturbed by bioturbation (Fig. 9E, F). Scoured surfaces and downlapping laminae were observed (Fig. S4A).

#### 4.1.7. Banded dark gray muddy siltstone

The banded dark gray muddy siltstone facies, comprised of more clay minerals (40–46%) and less detrital quartz (30–39%) than deposits of the banded gray muddy siltstone facies is present in both cores though it is thickest in the Xiye-1 core (Fig. 3). It typically comprises a succession of silty bands, bundles of parallel silt laminae, and clay-rich layers (Fig. 10A, B). Contacts among these units are sharp (Fig. 10B, C), silty bands appear upgraded (Fig. 10C). However, the abundance of silt within given bands can be quite variable (Fig. 10C, D). Some silty bands appear to have been homogenized by bioturbation. Scouring surfaces and ripple laminae are also observed (Fig. 10C).

#### 4.2. C and S isotopes and organic carbon content

$\delta^{13}\text{C}_{\text{org}}$  values of the Tongye-1 core display a narrow range from  $-30.85$  to  $-28.32\text{‰}$  (Fig. 11; Table 1). However, these values appear to partly reflect facies type. The  $\delta^{13}\text{C}_{\text{org}}$  values of bioturbated claystone and faintly banded black siliceous shale of the Wufeng Formation range from  $-30.85$  to  $-30.30\text{‰}$ . Isotopic values of the muddy fossiliferous facies of the Guanyinqiao Formation display a positive excursion of approximately 2‰ from the underlying strata. Up-section from the muddy fossiliferous facies of the Tongye-1 core, however,  $\delta^{13}\text{C}_{\text{org}}$  values of faintly banded black shale of the Longmaxi Formation diminish to low values, ranging from  $-30.34$  to  $-29.71\text{‰}$  (Fig. 11).  $\delta^{13}\text{C}_{\text{org}}$  values of the overlying banded gray muddy siltstone display a weak positive excursion (Fig. 11).  $\delta^{13}\text{C}_{\text{org}}$  values of the Xiye-1 core diminish upward from the basal bioturbated claystone ( $-29.55\text{‰}$ ) into overlying faintly banded black siliceous shale ( $-30.98\text{‰}$ ) (Fig. 12). It is noteworthy that unlike the Tongye-1 core, the Xiye-1 core displays only a subtle positive excursion of  $+0.7\text{‰}$  corresponding with the muddy fossiliferous facies

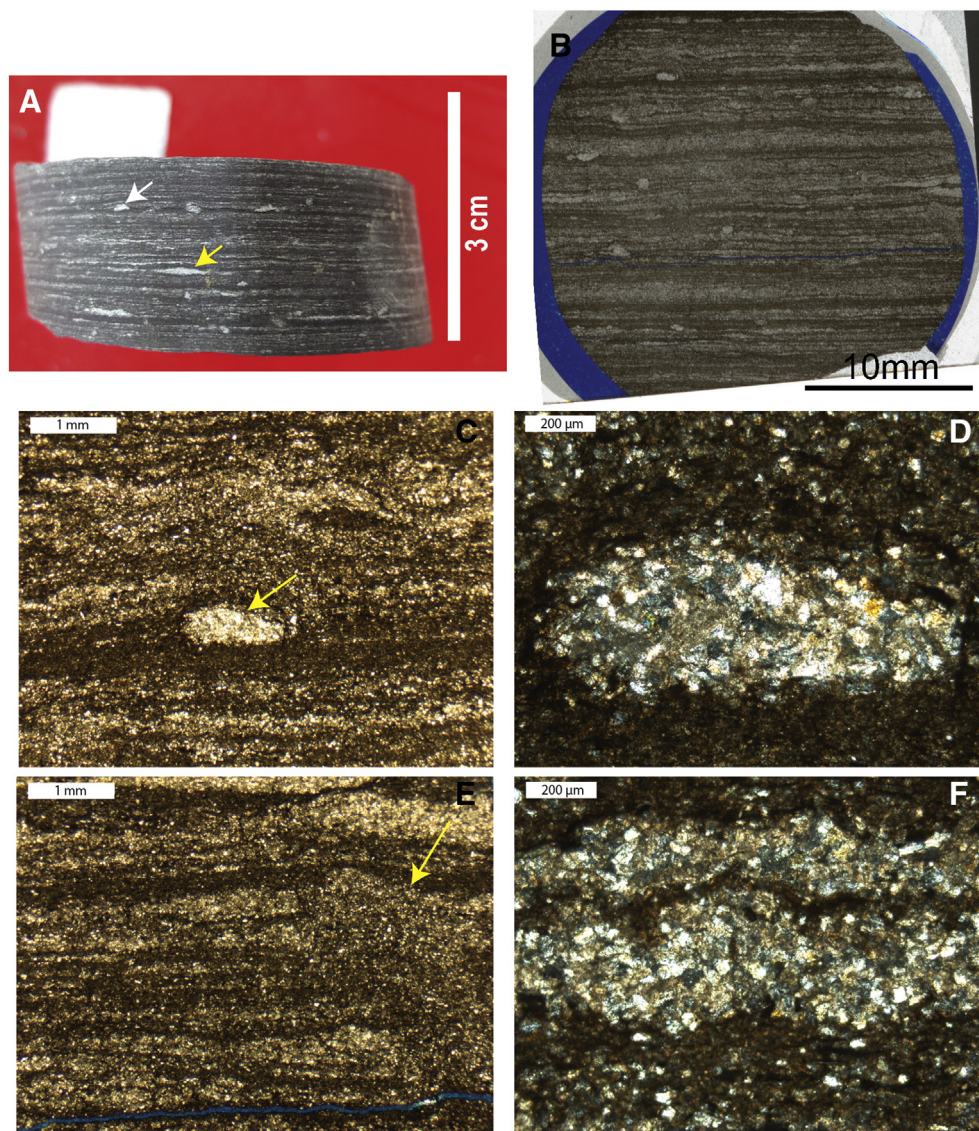


**Fig. 9.** Sedimentary features of the upper part of the banded gray muddy siltstone of the Tongye-1 core. (A) Longitudinal view of core sample TY-7 (649.8 m). Silt bands become thinner. White arrow points to a burrow. Yellow arrow indicates wavy-lenticular lamina. (B) Photomicrograph of sample TY-7. Note distributions of burrows. (C) Micrograph of silt bands interbedded with clay-rich layers. Yellow arrow indicates a burrow. (D) Close-up of the burrow (cross-polarized light). The silty burrow is cemented by diagenetic carbonate. (E) Micrograph of silt bands interrupted by bioturbation. Yellow arrow indicates bioturbation. (F) Close-up of a silt band (cross-polarized light) containing diagenetic carbonate cement. (For interpretation of the references to color in this figure legend, the reader is referred to the web version of this article.)

of the Guanyinqiao Formation (Fig. 12). There is a strong positive excursion in the middle of the Longmaxi Formation, rising from  $-30.52\%$  in faintly banded black shale to  $-21.18\%$  in overlying faintly banded black dolomitic siltstone (Fig. 12). The  $\delta^{13}\text{C}_{\text{org}}$  values of faintly banded black siliceous shale and faintly banded black shale are low, ranging from  $-30.98$  to  $-30.51\%$  (Fig. 12). In contrast, the  $\delta^{13}\text{C}_{\text{org}}$  values of the banded dark gray muddy siltstone are relatively high, ranging from  $-29.75$  to  $-29.81\%$  (Fig. 12).

$\delta^{34}\text{S}_{\text{sulfide}}$  values of the Tongye-1 core range from  $-28.77$  to  $+15.03\%$  (Fig. 11; Table 1). The  $\delta^{34}\text{S}_{\text{sulfide}}$  values diminish upward from  $-12.99\%$  in the bioturbated claystone into  $-28.77\%$  in the faintly banded black siliceous shale (Fig. 11). The  $\delta^{34}\text{S}_{\text{sulfide}}$  values show a trend of upwards increase in the faintly banded black siliceous shale, over a range from  $-28.77$  to  $-7.01\%$ . The muddy fossiliferous facies of the Guanyinqiao Formation displaying increasing  $\delta^{34}\text{S}_{\text{sulfide}}$  values from its base to the middle of the unit followed by a reduction of  $\delta^{34}\text{S}_{\text{sulfide}}$  into the overlying faintly banded black shale and banded gray muddy siltstone (Fig. 11). The Xiye-1 core displays a positive excursion associated with the bioturbated claystone of the middle part of the

Wufeng Formation (Fig. 12). A positive excursion of  $+5.74\%$  corresponds with the muddy fossiliferous facies (Fig. 12). Except for a weak negative isotope shift in faintly banded black dolomitic siltstone ( $+3.42$  to  $-6.16\%$ ),  $\delta^{34}\text{S}_{\text{sulfide}}$  increases up-section in the Longmaxi Formation from the faintly banded black siliceous shale to the faintly banded black shale (Fig. 12). The  $\delta^{34}\text{S}_{\text{sulfide}}$  data in the banded dark gray muddy siltstone display little variation, ranging from  $-6.67$  to  $-7.19\%$ .

TOC values of the Tongye-1 core are comparatively high in the bioturbated claystone and faintly banded black siliceous shale of the Wufeng Formation ( $4.17$ – $6.61\%$ ), as well as the faintly banded black shale of Longmaxi Formation ( $5.11$ – $9.10\%$ ) (Fig. 11; Table 1). Organic matter is less abundant in most samples (except for sample TY-3a) recovered from the muddy fossiliferous facies of the Guanyinqiao Formation ( $0.66$ – $0.96\%$ ) and from the banded gray muddy siltstones of the Longmaxi Formation ( $0.50\%$ ) (Fig. 11). TOC values of the Xiye-1 core are relatively low in the bioturbated claystone ( $1.15$  to  $1.30\%$ ). In contrast, TOC of the faintly banded black siliceous shale, faintly banded black shale and muddy fossiliferous facies are comparatively high with

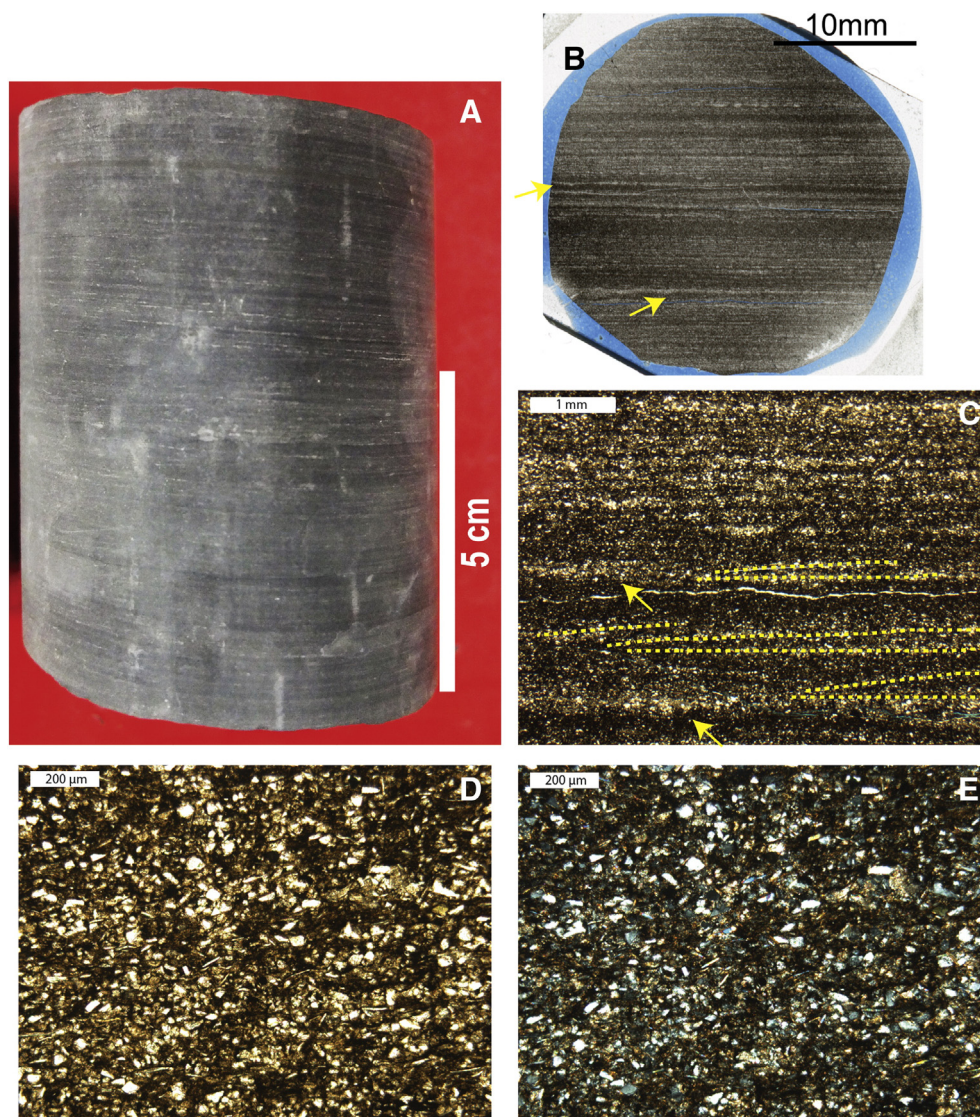


**Fig. 10.** Sedimentary features of the banded dark gray muddy siltstone. (A) Longitudinal view of core sample XY-14 (624.75 m). Note bundled silt laminae and thick silt bands. (B) Photomicrograph of sample XY-14. Silt bands are interbedded with clay-rich layers. Yellow arrows point to scouring surfaces. (C) Close-up of silt bands interbedded with clay-rich layers. Dashed yellow lines indicate low-angle laminae. Plane-polarized light image (D) and cross-polarized light image (E) of a silt band. The portion of detrital silts is relatively low when compared to banded gray muddy siltstone. (For interpretation of the references to color in this figure legend, the reader is referred to the web version of this article.)

a range of 2.69 to 5.77%. TOC of the banded dark gray muddy siltstone of the Longmaxi Formation range from 0.96 to 1.23%. Overall, TOC values do not show apparent correlation with  $\delta^{13}\text{C}_{\text{org}}$  data (Fig. 13A). In contrast, an obviously negative relationship between TOC and  $\delta^{34}\text{S}_{\text{sulfide}}$  data is observed (Fig. 13B).

## 5. Discussion

### 5.1. Depositional setting

The Katian-aged shales of the Wufeng Formation are considered to have accumulated in a silled epicontinental basin (e.g. Chen et al., 1987; Rong and Chen, 1987) in association with an incursion of anoxic bottom-water conditions (Chen et al., 2004; Yan et al., 2010, 2012) caused by the Boda global event (e.g. Armstrong et al., 2009; Brechley and Storch, 1989; Fortey and Cocks, 2005). However, the presence of completely bioturbated claystone (BI = 5) in the basal Wufeng Formation (Fig. 5C), indicates the establishment of oxygenated conditions ( $>5 \text{ mg L}^{-1}$ ; Dashtgard et al., 2015) and low sedimentation rates (MacEachern et al., 2010) early in the transgression, thereby

invalidating the existence of persistent anoxia. Further, the widespread occurrence of marcasite grains in deposits of the bioturbated claystone facies (Fig. 5G) likely reflects the pervasive re-oxidation of pyrite under oxic condition (Li and Schieber, 2015; Reaves, 1986; Schieber, 2007, 2011a). This facies has also been described from localities in Yibin, Sichuan Province, 100 km west of Xiye-1 core (Wu, 2016), which reveals the widespread nature of deposits that accumulated under oxygenated conditions at this time. Bioturbated claystone facies deposits reflect oxic muddy shelf conditions of comparatively low clastic input and limited reworking so that benthic fauna was able to extensively homogenize the primary sedimentary fabric of water-rich surface muds (Figs. 5, 14A). Overlying faintly banded black siliceous shale is characterized by minor bioturbation (Fig. 6) and high TOC. Low BI values are associated with elevated physico-chemical stress, which could reflect high sedimentation rates, high bottom-water energy, low dissolved-oxygen levels in bottom water, brackish water, and/or limited food supply (MacEachern et al., 2010; Gingras et al., 2011). Bands in organic-rich sediments are results from meiofaunal activity, and low sedimentation rates will produce very blurry contacts (Riese, 2014). Thus, the faintly banded black siliceous shale appears to have been deposited

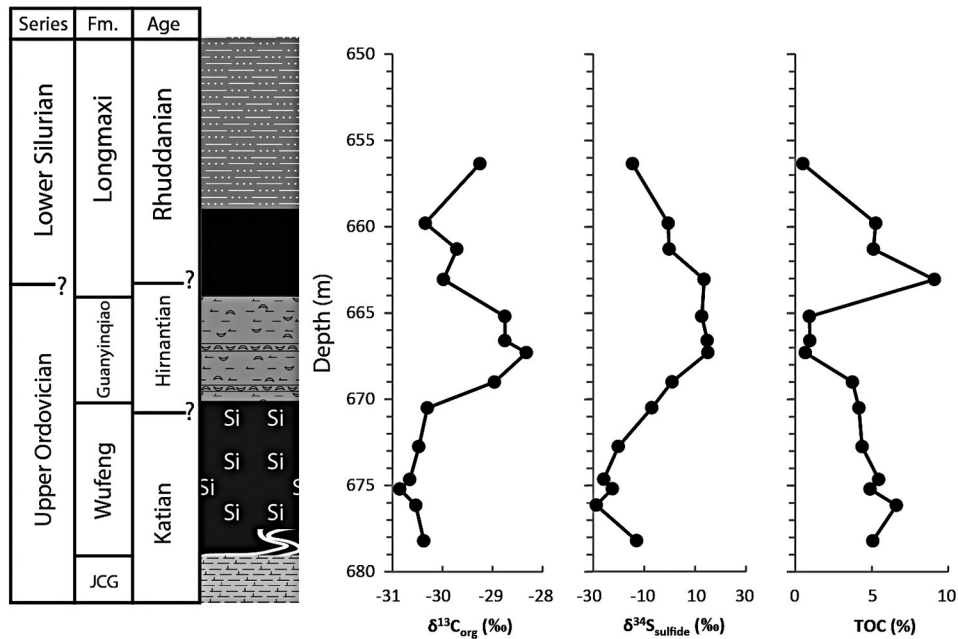


Fig. 11. Stratigraphic variation of  $\delta^{13}C_{org}$ ,  $\delta^{34}S_{sulfide}$ , and TOC across the Ordovician to Silurian contact, Tongye-1 core. JCG: Jiancaogou.

at low sedimentation rates under quiet bottom-water conditions and relatively high paleoproductivities (indicated by biogenic barium, Li et al., 2015b; Zhou et al., 2015). In addition, salinity remained relatively stable in the deposits of Wufeng Formation (Li et al., 2015b). Hence, the minimally bioturbated nature of this facies suggests limited dissolved oxygen in the depositional environment (e.g. Diaz and Rosenberg, 1995; Ekdale and Mason, 1988; Savrda, 2007; Savrda and Bottjer, 1991). The combination of high TOC, diminished detrital flux (low proportion of clay minerals) and enriched authigenic quartz within deposits of the faintly banded black siliceous shale facies probably be attributed to the establishment of sediment starved conditions (Fig. 6E, F) (Schieber, 1996; Schieber et al., 2000), allowing the accumulation in pore spaces of diagenetic silica derived from dissolution of radiolaria tests (Fig. 6D). Faintly layered, poorly sorted deposits are typically considered to reflect settling of sediment from suspension (Fig. 6A, B) (Loucks and Ruppel, 2007; Stow et al., 2001). The faunal community

representing Benthic Assemblage 4–5 (BA4–5, sensu Boucot, 1975) (Rong, 1979, 1984; Rong and Chen, 1987; Rong et al., 2002) indicates a water depth of 100–200 m. The presence of these types of deposits in the Wufeng Formation has been attributed to slow pelagic accumulation in an oxygen-depleted water column of a stratified basin (e.g. Yan et al., 2012; Chen et al., 2004). However, the presence of widespread flattened silt/clay peloids suggests otherwise. A carbonaceous laminated sediment results in which fecal pellets are the only indication of the former presence of deposit-feeding polychaete worms (Cuomo and Rhoads, 1987). Benthic fecal pellets are dominated by silt, clay, and organic matter, whereas zooplankton fecal pellets contain abundant biogenic components (Cuomo and Bartholomew, 1991). Flattened silt/clay peloids observed within the faintly banded black siliceous shale facies (Fig. 6C, D) compared closely to benthic fecal pellets described from Devonian black shales (Cuomo and Bartholomew, 1991; Cuomo and Rhoads, 1987; Lazar, 2007; Schieber, 1999) likely reflect the

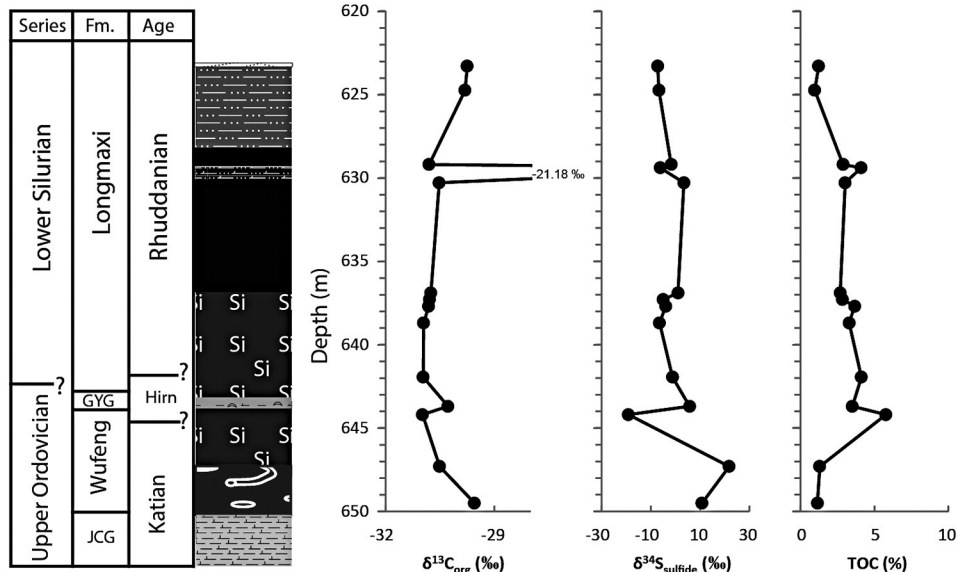
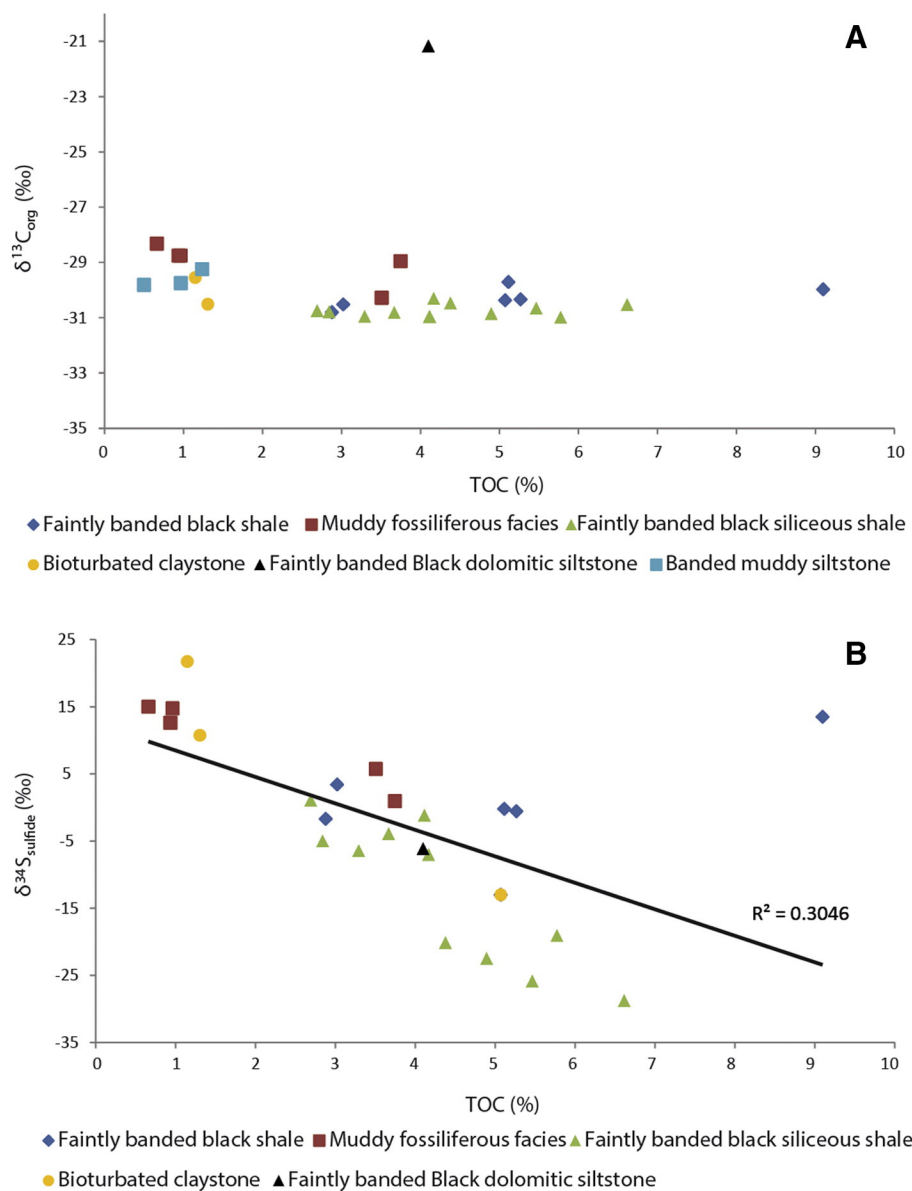


Fig. 12. Stratigraphic variation of  $\delta^{13}C_{org}$ ,  $\delta^{34}S_{sulfide}$ , and TOC across the Ordovician to Silurian contact, Xiye-1 core. JCG: Jiancaogou; GYG: Guanyinqiao; Hirn: Hirnantian.



**Fig. 13.** Plots of TOC (%) against  $\delta^{13}\text{C}_{\text{org}}$  (‰) (A) and  $\delta^{34}\text{S}_{\text{sulfide}}$  (‰) (B). Various facies in these two wells are indicated. Note the banded muddy siltstone including banded gray muddy siltstone and banded dark gray muddy siltstone.

existence of benthic life under dysoxic conditions. In addition, neochronology experiments with nematodes demonstrate that banded fabric represents the continued presence of small metazoans and of dissolved oxygen (Riese, 2014). Thus, protracted widespread anoxia is not supported; instead, it is likely that anoxia was interrupted by episodes of dysoxia, perhaps seasonal (Tyson and Pearson, 1991). In summary, the depositional setting of the Wufeng Formation of the northwestern Guizhou region of South China probably evolved from a shallow oxic muddy shelf to a deeper starved shelf (Fig. 14A).

The Hirnantian Guanyinqiao Formation has been interpreted to reflect deposition of cool water carbonate deposition (indicated by cold/cool-water benthic fauna, Rong et al., 2002) as a consequence of global glacial events (e.g. Chen et al., 2004; Yan et al., 2009, 2012; Fan et al., 2009). This episode of continental-scale glaciation occurred during Early to Middle-Hirnantian times and includes two major phases of ice advance and retreat (e.g. Melchin et al., 2013; Mitchell et al., 2011; Schönlaub et al., 2011; Moreau, 2011). The sea-level lowstand during which the muddy fossiliferous facies of the Guanyinqiao Formation accumulated was accompanied by improved oxygen levels caused by persistent agitation of the water column. The common observation of

secondary marcasite probably reflects a post-depositional downward oxidation (Schieber, 2007, 2011a) which is called “burn-down” event. Further, reduced chemical weathering rates (cold and dry climate) and growth of continental ice cover during the Hirnantian lead to diminished continental weathering flux (Yan et al., 2010; Finlay et al., 2010; Holmden et al., 2013; Desrochers et al., 2010), which favors the production of epifaunal carbonates (Chen et al., 2004). The amount of carbonate production is thought to have been relatively low (Copper, 2001), and the Guanyinqiao Formation is considered to be an unconventional condensed bed (Chen et al., 2004). The muddy fossiliferous facies varies in appearance from proximal to distal (Figs. 7, 14B, S1). Proximal muddy fossiliferous facies deposits present in the Tongye-1 core may have accumulated in comparatively shallow water and show various background matrix (Figs. 7, 14B, S1). Abundant coarse silt-size in the lower muddy fossiliferous facies (Fig. 7) may record the onset of glaciation and the transition from a modestly deep starved shelf to a shallow shelf. The presence of wavy beds (Fig. 7A) may tell of sediment re-working by storms. Overlying deposits are characterized by bioturbated mud-rich micrite (Fig. S1A, B) and non-bioturbated micrite successively (Fig. S1E), possibly reflecting a reduction of fine-grained

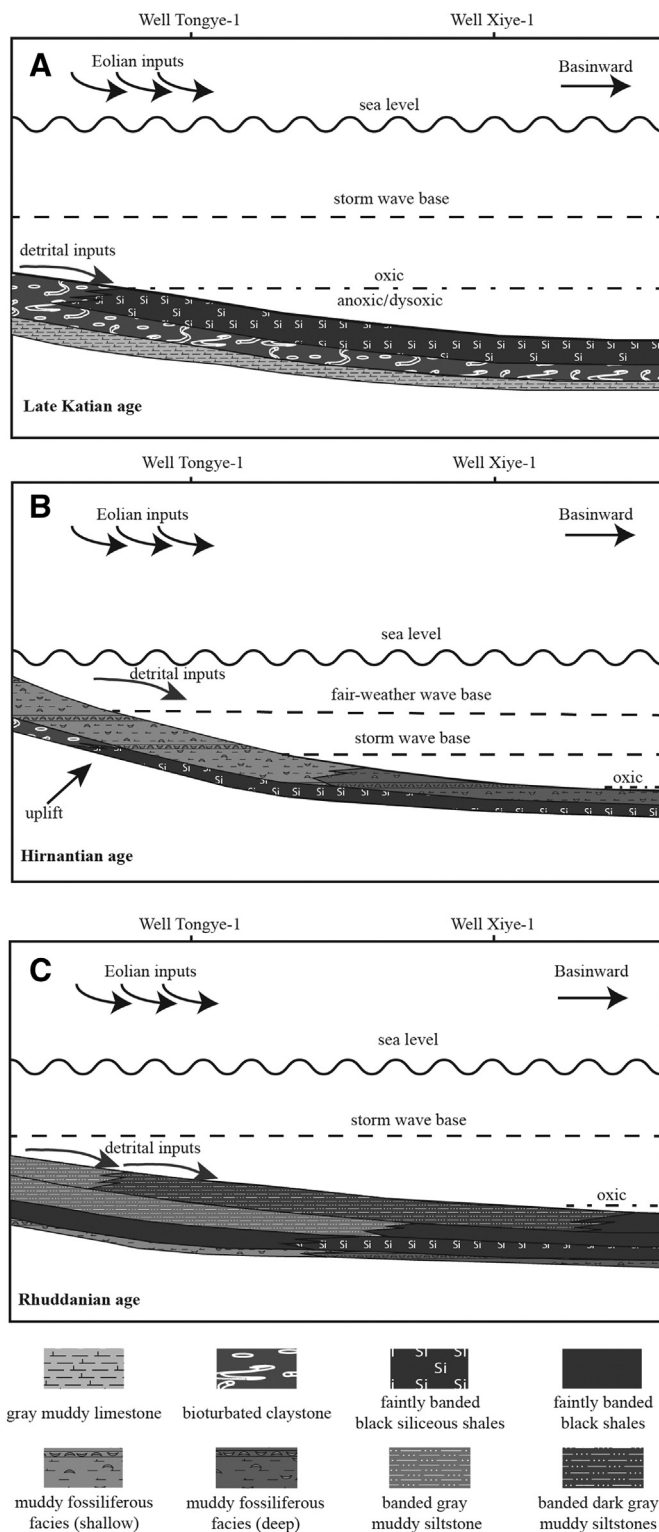


**Fig. 14.** Schematic facies distribution for (A) the Late Katian age, (B) the Hirnantian age, and (C) the Rhuddanian age, northwestern Guizhou. Note: figures not drawn to scale.

sediment input during the peak of the glaciation. Occasional shelly fauna-rich layers within the muddy fossiliferous facies contain diagenetic phosphate and phosphatic pellets (Fig. S1D) may be condensed layers that accumulated during brief periods of ice-sheet retreat (e.g. Melchin et al., 2013; Mitchell et al., 2011; Schönlaub et al., 2011; Moreau, 2011). Enrichment of the distal muddy fossiliferous facies observed in the Xiye-1 core in diagenetic silica and calcite may reflect a diminished effect of glaciation in the distal, deeper areas of the basin (Fig.

14B). Further, the presence of an in situ benthic fauna (Fig. 8B) suggests that the distal muddy fossiliferous facies was deposited in oxygenated bottom water. Overall, the typical *Hirnantia* shelly fauna in Guanyinqiao Formation is a relatively shallow water fauna representing BA2–3 (Rong and Chen, 1987; Rong et al., 2002), which indicates a water depth of 20–30 m (Zhang et al., 2016).

The latest Hirnantian (middle part of the late Hirnantian *M. persculptus* Zone) to early Rhuddanian time interval is widely regarded as a period of glacial retreat and consequent transgression (e.g. Brenchley et al., 1994; Kaljo et al., 2011; LaPorte et al., 2009; Moreau, 2011). The organic-rich lower Longmaxi Formation is interpreted to have accumulated in oxygenated depleted conditions established in response to global transgression (e.g. Chen et al., 2004; Yan et al., 2012). However, the presence of flattened fecal pellets casts doubt on a perceived anoxic Yangtze sea as proposed by Chen et al. (2004) and Yan et al. (2012). The basal Longmaxi Formation in the distal area (Xiye-1 well) consists of faintly banded black siliceous shale that probably accumulated under sediment starved conditions. The basal Longmaxi Formation Tongye-1 core is characterized by faintly banded black shale rather than faintly banded black siliceous shale, suggesting a comparatively higher supply of clastics (Figs. 14C, S2). In addition, the absence of the basal *A. ascensis* and *P. acuminatus* graptolite Zones in the proximal Tongzi area (Fig. 4) suggests a short non-depositional or erosional period related to uplift of a submarine bathymetric high (Rong et al., 2011). Lowering sea level was accompanied by a transition from faintly banded black shale into banded gray muddy siltstone (Figs. 14C, S4) and increasing clastic supply. Silty bands and silty laminae or ripples interbedded with clay-rich layers probably reflect bedload transport by unidirectional bottom currents (Figs. 9A, S4A) (Schieber, 2016). Recent flume experiments (Schieber, 2011c; Schieber et al., 2007; Schieber and Southard, 2009; Schieber and Yawar, 2009) demonstrate that ripples in muddy and sandy sediments can form under similar velocity range (15 to 35 cm/s). Moreover, intermingled silt-rich and clay-rich laminae probably result from the segregation of coarse silt from the finer particles during bedload transport (Schieber, 2011c), which can be produced by tidal and wind driven circulation (Schieber, 2016). Bedload transport of mud by bottom currents is the principal transport process in the distal offshore deposits of epicontinental shale successions. However, textural evidence of bioturbation of tiny worms (such as nematodes; Pike et al., 2001) (Fig. 9C–F) suggests lower sedimentation rates and fewer episodes of bottom current activity (MacEachern et al., 2010). Correlation of gamma ray profiles suggests that gray muddy siltstone of the proximal area is the lateral equivalent of faintly banded black shale facies deposits of the distal area (Figs. 3, 14C). The uppermost facies of the Longmaxi Formation includes banded dark gray muddy siltstone in both proximal and distal wells (Figs. 3, 14C) suggestive of bedload transport. Diminished silt contents of these deposits relative to underlying strata are suggestive of lower sedimentation rates and/or higher sea level (Fig. 10). The lateral continuity of the banded dark gray muddy siltstone facies from proximal to distal areas probably suggests that previously existing bathymetric contrasts in the vicinity of the Tongye-1 well have disappeared and the paleogeomorphology was rather flat by this time (Fig. 14C).

### 5.2. C-cycling process

Positive  $\delta^{13}\text{C}$  (both  $\delta^{13}\text{C}_{\text{carb}}$  and  $\delta^{13}\text{C}_{\text{org}}$ ) excursions of Hirnantian age have been reported from sections of the Yangtze Platform (e.g. Fan et al., 2009; Gorjan et al., 2012; Liu et al., 2016, 2017; Yan et al., 2009; Zhang et al., 2009) as well as from various localities worldwide (e.g. Jones et al., 2011; Kaljo et al., 2011; Kump et al., 1999; LaPorte et al., 2009; Melchin and Holmden, 2006). The global nature of the Hirnantian positive  $\delta^{13}\text{C}$  excursion been attributed to glaciation (e.g. Brenchley et al., 2003; Delabroye and Vecoli, 2010; Melchin et al., 2013; Munnecke et al., 2010). One school of thought holds that glaciation was accompanied by a global increase of primary productivity and consequent elevated

organic burial which induced a reduction of atmospheric  $p\text{CO}_2$  leaving the ocean reservoir isotopically heavy (e.g. Brechley et al., 2003, 1994; Marshall et al., 1997; Marshall and Middleton, 1990); Alternatively, a global regression stemming from the expansion of polar ice and enhanced weathering of the exposed low latitudes carbonate platforms causing a higher proportion of weathered carbonate to be contributed to the world ocean (e.g. Kump et al., 1999; Melchin and Holmden, 2006).

The enhanced organic burial hypothesis might not be responsible for the positive  $\delta^{13}\text{C}_{\text{org}}$  excursion documented in the present study. If an enhanced organic carbon burial causes a positive shift of  $\delta^{13}\text{C}_{\text{org}}$ , organic-rich deposits should be observed in the Hirnantian interval. Data from the sections of the present study as well as other sections on the Yangtze Platform (e.g. Wangjiawan and Nanbazi sections) exhibit relatively low TOC values in the Hirnantian equivalent (e.g. Gorjan et al., 2012; Yan et al., 2009). Further, sediments from the Hirnantian glacial interval are characterized globally by lower concentrations of organic matter compared to overlying and underlying strata (e.g. Melchin and Mitchell, 1991; Hallam and Wignall, 1999; Melchin and Holmden, 2006), suggesting a scenario more consistent with decreased, as opposed to increased, rates of organic carbon burial. In addition, there are no stratigraphic sections that transition from a more oxic depositional setting in the late Katian to an anoxic setting in the Hirnantian worldwide (summarized by Melchin et al., 2013). These observations suggest that enhanced organic matter burial may be not responsible for the positive shift of  $\delta^{13}\text{C}_{\text{org}}$  excursion. The carbonate weathering model postulated by Kump et al. (1999) is supported by the global association of positive  $\delta^{13}\text{C}$  excursion, especially  $\delta^{13}\text{C}_{\text{carb}}$ , coincident with the Hirnantian regression. The strong positive  $\delta^{13}\text{C}_{\text{org}}$  excursion coincident with the Hirnantian Guanyinqiao Formation of the Tongye-1 core (Fig. 11) may reflect increased carbonate weathering during the Hirnantian glacial event. However, analysis of the Xiye-1 core reveals only a subtle positive  $\delta^{13}\text{C}_{\text{org}}$  excursion of Hirnantian age (Fig. 13; Table 1). Although the Hirnantian interval is only represented by a single data point in the Xiye-1 core,  $\delta^{13}\text{C}_{\text{org}}$  data of other distal section of the Yangtze Platform also display a weak positive shift in the Hirnantian (Liu et al., 2016). It is noteworthy that the very strong positive  $\delta^{13}\text{C}_{\text{org}}$  excursion in faintly banded black dolomitic siltstone of the Longmaxi Formation of the Xiye-1 core is not coincident with known glacial events (Fig. 12; Table 1), nor does it correlate with isotope excursions from elsewhere in the world (e.g. Kump et al., 1999; LaPorte et al., 2009; Melchin and Holmden, 2006). Thus, glacial events may not be a unique pathway for variation of  $\delta^{13}\text{C}_{\text{org}}$  values in the different depositional settings.

Melchin and Holmden (2006) suggest that magnitude differences between Hirnantian  $\delta^{13}\text{C}_{\text{org}}$  excursions in shallower and deeper water successions of epicontinental basins may record isotopic overprinting by local C-cycling. The higher magnitude excursions documented from proximal settings may reflect: (1) enhanced influences of local carbonate weathering fluxes and (2) restricted carbon exchanges between epicontinental seas and the global ocean (Melchin and Holmden, 2006). Moreover, increased photosynthetic activity in nearshore regions may also contribute to the evaluated sedimentary  $\delta^{13}\text{C}$  values (LaPorte et al., 2009). Nevertheless,  $\delta^{13}\text{C}$  records from the Ely Springs Dolostone display a relative low magnitude of the excursion in shallow shelf section, which does not support the weathering hypothesis (Jones et al., 2016). Alternatively, variation of  $\delta^{13}\text{C}_{\text{org}}$  values might be related to proximal-to-distal variation of depositional environment. Muddy fossiliferous facies and banded gray muddy siltstone of the Tongye-1 core show higher  $\delta^{13}\text{C}_{\text{org}}$  values than faintly banded black shale and faintly banded black siliceous shale which reflect deep water environment (Fig. 11). Similarly, bioturbated claystone and banded dark gray muddy siltstone are characterized by heavier  $\delta^{13}\text{C}_{\text{org}}$  values than faintly banded black shale and faintly banded black siliceous shale of the Xiye-1 core (Fig. 12; Table 1). Unlike well Tongye-1, the great abundance of siliceous shale as the matrix of the muddy fossiliferous facies of the Xiye-1 core reflects relatively deeper environment and displays relatively

lighter  $\delta^{13}\text{C}_{\text{org}}$  values (Fig. 12; Table 1). This facies-related variation of  $\delta^{13}\text{C}_{\text{org}}$  values may reflect mixing of two spatially separated organic matter reservoirs through the two-component end-member mixing model (Ahm et al., 2017; Johnston et al., 2012). The shallow end-member is shallow-water facies with relatively heavier  $\delta^{13}\text{C}_{\text{org}}$  values ( $> -30\text{‰}$ ) and low TOC contents, and the deep end-member is deep-water facies with lower  $\delta^{13}\text{C}_{\text{org}}$  values ( $< -30\text{‰}$ ) and high concentrations of TOC. The mixing of these two end-members would lead to non-linear correlation between  $\delta^{13}\text{C}_{\text{org}}$  and TOC, which matches the observation from the Wufeng-Longmaxi succession (Fig. 13A). Further, the mixing model probably reflects spatial gradients in seawater  $\delta^{13}\text{C}_{\text{DIC}}$  (Ahm et al., 2017). Ahm et al. (2017) suggest that the open ocean Hirnantian carbon isotope excursion amount to only  $\sim +1.5\text{‰}$   $\delta^{13}\text{C}_{\text{DIC}}$ , which is consistent with subtle positive  $\delta^{13}\text{C}_{\text{org}}$  excursion in the distal section (Fig. 12). In shallow water environments, however, increased glacio-eustatic restriction may strengthen spatial gradients in seawater  $\delta^{13}\text{C}_{\text{DIC}}$  and cause the significant excursion in the proximal section (Fig. 11). The extremely high  $\delta^{13}\text{C}_{\text{org}}$  value ( $-21.18\text{‰}$ ) of faintly banded black dolomitic siltstone of the Xiye-1 core (Fig. 12) may not reflect typical fractionation of carbon isotopes by phytoplanktonic producers. Given the high TOC content of this facies, the dolomite is probably early diagenetic in nature. Degradation of organic matter promotes early dolomite precipitation by simultaneously increasing the carbonate alkalinity and lowering the sulfate ion concentration to near zero (Compton, 1988). Authigenic carbonate precipitation fueled by early diagenetic methanogenesis would produce dissolved inorganic carbon with higher  $\delta^{13}\text{C}$  than primary sediment (Hoefs, 2008; Jones et al., 2016).

### 5.3. S-cycling mechanism

$^{34}\text{S}$  is enriched in the sulfate relative to the sulfide because of the relative ease of breaking  $^{32}\text{S}-\text{O}$  bond relative to the  $^{34}\text{S}-\text{O}$  bond in association with such processes such as bacterially mediated reduction of dissolved sulfate to sulfide (e.g. Canfield, 2001; Seal, 2006). The isotopic composition of sulfide is largely controlled by the isotopic composition of the source sulfate and the magnitude of fractionation. The magnitude of fractionation is influenced by a number of factors, including (1) metabolic activity (Canfield, 2001; Ingvorsen and Jørgensen, 1984); (2) sulfate reduction rate (Berner, 1984; Canfield, 2001; Habicht and Canfield, 1997, 2001); (3)  $\text{H}_2$  as an electron donor (Canfield, 2001; Chambers et al., 1975; Kaplan and Rittenberg, 1964); and (4) the number of sulfur cycles (Canfield, 2001; Habicht and Canfield, 1997, 2001).

A few sections of the Yangtze Platform (e.g. Wangjiawan, Nanbazi, and Honghuayuan) display a Hirnantian positive  $\delta^{34}\text{S}_{\text{sulfide}}$  excursion (Gorjan et al., 2012; Liu et al., 2017; Yan et al., 2009; Zhang et al., 2009). Yan et al. (2009) attribute heavier  $\delta^{34}\text{S}_{\text{sulfide}}$  values associated with the Guanyinqiao Formation to a transition from anoxic to oxic bottom-water conditions and consequent reduced bacterial sulfate reduction rate. Alternatively, sediment of the Guanyinqiao Formation were deposited in a restricted sub-basin, progressive bacterial sulfate reduction would lead to sulfate in the seawater being enriched in  $\delta^{34}\text{S}$ , subsequently resulting in heavier  $\delta^{34}\text{S}_{\text{sulfide}}$  (Zhang et al., 2009). Recently, Jones and Fike (2013) suggest that this global  $\delta^{34}\text{S}_{\text{sulfide}}$  excursion can be caused by a transient reduction in isotopic fractionations during microbial sulfur cycling ( $\varepsilon_{\text{pyr}}$ ) in response to changing environmental factors (e.g. redox conditions and syndepositional reworking processes). Both sedimentary reworking and bioturbation can allow partial or complete oxidation of the reduced sulfur pools (e.g. Aller et al., 2010; Fike et al., 2015). Under such conditions, microbial sulfate reduction would occur within sediments. Lack of free sulfate exchange between pore waters and the overlying water column would result in  $\delta^{34}\text{S}$ -enrichment sulfide minerals forming within the sediment (e.g. Maynard, 1980; Migdisov et al., 1983; Jones and Fike, 2013). This mechanism is consistent with the robust association of relatively heavy  $\delta^{34}\text{S}_{\text{sulfide}}$  values and bioturbated claystones as well as muddy fossiliferous facies that

accumulated in oxic conditions (Figs. 11 and 12). Hirnantian muddy fossiliferous facies of the Tongye-1 core that accumulated in agitated water column with episodic reworking processes displays the obvious positive  $\delta^{34}\text{S}_{\text{sulfide}}$  excursion ( $\sim +5.06\%$ ), which is consistent with the hypothesis mentioned above (Fig. 11). On the other hand, the distal muddy fossiliferous facies, by virtue of its relatively deeper environment of deposition and lower oxygen level, experienced fewer physical reworking processes yielding only a subtle  $\delta^{34}\text{S}_{\text{sulfide}}$  excursion (Fig. 12). Such significant changes in the magnitude of the positive shift in  $\delta^{34}\text{S}_{\text{sulfide}}$  values between shallower- and deeper-water sections in the Yangtze Platform have also been indicated by previous studies (Yan et al., 2009; Zhang et al., 2009). The apparent inconsistency of  $\delta^{34}\text{S}_{\text{sulfide}}$  excursions in Hirnantian proximal and distal deposits may reflect a fundamental heterogeneity of depositional environment that exerts significant control on biogeochemical processes involving sulfur. It is important to note that, the faintly banded black siliceous shales of Wufeng Formation display relatively light  $\delta^{34}\text{S}_{\text{sulfide}}$  values ( $-28.77$  to  $-7.01\%$ ), whereas the faintly banded black siliceous shales or black shales of Longmaxi Formation are characterized by relatively heavy  $\delta^{34}\text{S}_{\text{sulfide}}$  records ( $-6.45$  to  $1.05\%$ ). These facies, however, were deposited under similar depositional conditions (anoxic/dysoxic conditions and low bottom water energy). The relatively heavier  $\delta^{34}\text{S}_{\text{sulfide}}$  values of the facies in the Longmaxi Formation may reflect increased cell-specific sulfate reduction rates, as compared to the sediments in the Wufeng Formation. This enhanced sulfate reduction rates might be caused by increased availability of labile organic substrates (Leavitt et al., 2013; Sim et al., 2011), although more work is needed to support this hypothesis. Overall,  $\delta^{34}\text{S}_{\text{sulfide}}$  values show generally negative covariance with TOC, exclusive of the dark gray muddy siltstone and the gray silty shale facies (Fig. 13B). Given that the enrichment of organic matter is partly controlled by redox conditions and bottom water energy (Canfield, 1989; Wignall, 1991), the negative relationship further demonstrates that redox conditions as well as physically reworking processes of bottom water mainly control microbial sulfate reduction and associated fractionation of sulfide.

## 6. Conclusions

The present study of two cores spanning the Ordovician–Silurian boundary of the Yangtze Platform of South China suggests that bioturbated claystone of the basal Wufeng Formation accumulated under oxic conditions at the beginning of Boda transgression event. Overlying faintly banded black siliceous shale records a history of slow accumulation of organic matter and minor clastic input. The presence of flattened silt/clay peloids, likely benthic fecal pellets, tells of repeated dysoxic events thereby challenging the concept of a persistently anoxic ocean during late Katian times. The muddy fossiliferous facies of the Hirnantian Guanyinqiao Formation appears to record a glacially induced sea-level lowstand. Observed lateral heterogeneity of this unit from proximal to distal settings may be attributed to a submarine bathymetric high in the proximal area. The basal Longmaxi Formation appears to preserve the record of a post-glacial transgressive event during the latest Hirnantian to the earliest Rhuddanian transition. Rapidly deposited banded muddy siltstones at the top of the Longmaxi Formation were transported to more distal areas of the basin by bedload currents. Covariation of lithofacies and  $\delta^{13}\text{C}_{\text{org}}$  values suggests that local depositional environment exerted influence on carbon cycling. Differences between Hirnantian positive  $\delta^{13}\text{C}_{\text{org}}$  excursions in proximal and distal areas of the epicontinental sea may suggest strengthened spatial gradients in seawater  $\delta^{13}\text{C}_{\text{DIC}}$  driven by increased glacio-eustatic restriction. The observed negative co-variance of  $\delta^{34}\text{S}_{\text{sulfide}}$  and TOC in the studied two sections indicates that redox conditions as well as energy levels at the sediment–water interface influenced, to some extent, bacterial sulfate reduction and sulfur isotope fractionation. Specially, those facies deposited under oxic and physically dynamic condition display maximum positive excursions of  $\delta^{34}\text{S}_{\text{sulfide}}$  values, perhaps a consequence of the

greater burial depth at which sulfate reduction occurred thereby disconnecting the pore water from the seawater sulfate pool. Thus, regional variations of depositional environments may have exerted a fundamental control on isotopic geochemistry though more data are needed for further assessment of this question.

## Acknowledgments

The research is financially supported by National Key Project of China (2009GYXQ15-04), China Postdoctoral Science Foundation funded project (2017M610958), Natural Science Foundation of Jiangsu Province (BK20171103), and the Indiana University Shale Research Consortium. Thanks would go to China Scholarship Council for providing student support. Thanks would go to Dr. Thomas Algeo and two anonymous reviewers for their constructive suggestions. The authors would like to acknowledge Dr. Peter Sauer and Dr. Yongbo Peng for analysis of stable isotopic data.

## Appendix A. Supplementary data

Supplementary data to this article can be found online at <http://dx.doi.org/10.1016/j.palaeo.2017.07.039>.

## References

- Ahm, A.-S.C., Bjerrum, C.J., Hammarlund, E.U., 2017. Disentangling the record of diagenesis, local redox conditions, and global seawater chemistry during the latest Ordovician glaciation. *Earth Planet. Sci. Lett.* 459, 145–156.
- Algeo, T.J., Marenco, P.J., Saltzman, M.R., 2016. Co-evolution of oceans, climate, and the biosphere during the 'Ordovician Revolution': a review. *Palaeogeogr. Palaeoclimatol. Palaeoecol.* 1–11.
- Aller, R.C., Madrid, V., Chistoserdov, A., Aller, J.Y., Heilbrun, C., 2010. Unsteady diagenetic processes and sulfur biogeochemistry in tropical deltaic muds: implications for oceanic isotope cycles and the sedimentary record. *Geochim. Cosmochim. Acta* 74, 4671–4692.
- Armstrong, H.A., Baldini, J.U.L., Challands, T.J., Grocke, D.R., Owen, A.W., 2009. Response of the inter-tropical convergence zone to southern hemisphere cooling during Upper Ordovician glaciation. *Palaeogeogr. Palaeoclimatol. Palaeoecol.* 284, 227–236.
- Berner, R.A., 1984. Sedimentary pyrite formation: an update. *Geochim. Cosmochim. Acta* 48, 605–615.
- Bohacs, K.M., 2005. Production, destruction, and dilution—the many paths to source-rock development. In: Harris, N.B. (Ed.), *The Deposition of Organic-Carbon-Rich Sediments: Models, Mechanisms, and Consequences*. Society of Sedimentary Geology, Tulsa, Oklahoma, U.S.A., pp. 61–101.
- Bohacs, K.M., Lazar, O.R., Demko, T.M., 2014. Parasequence types in shelfal mudstone strata—quantitative observations of lithofacies and stacking patterns, and conceptual link to modern depositional regimes. *Geology* 42, 131–134.
- Boucot, A.J., 1975. *Evolution and Extinction Rate Controls: Developments in Paleontology and Stratigraphy*. vol. 1. Elsevier, Amsterdam, pp. 1873–1876 (1981).
- Brenchley, P.J., Storch, P., 1989. Environmental-changes in the Hirnantian (Upper Ordovician) of the Prague Basin, Czechoslovakia. *Geol. J.* 24, 165–181.
- Brenchley, P.J., Marshall, J.D., Carden, G.A.F., Robertson, D.B.R., Long, D.G.F., Meidla, T., Hints, L., Anderson, T.F., 1994. Bathymetric and isotopic evidence for a short-lived Late Ordovician glaciation in a greenhouse period. *Geology* 22, 295–298.
- Brenchley, P.J., Carden, G.A., Hints, L., Kaljo, D., Marshall, J.D., Martma, T., Meidla, T., Nölvak, J., 2003. High-resolution stable isotope stratigraphy of Upper Ordovician sequences: constraints on the timing of bioevents and environmental changes associated with mass extinction and glaciation. *Geol. Soc. Am. Bull.* 115, 89–104.
- Brüchert, V., 1998. Early diagenesis of sulfur in estuarine sediments: the role of sedimentary humic and fulvic acids. *Geochim. Cosmochim. Acta* 62, 1567–1586.
- Canfield, D.E., 1989. Sulfate reduction and oxic respiration in marine sediments: implications for organic carbon preservation in euxinic environments. *Deep Sea Res. Part A* 36, 121–138.
- Canfield, D.E., 2001. Biogeochemistry of sulfur isotopes. *Rev. Mineral. Geochem.* 43, 607–636.
- Chambers, L.A., Trudinger, P.A., Smith, J.W., Burns, M.S., 1975. Fractionation of sulfur isotopes by continuous cultures of *Desulfovibrio desulfuricans*. *Can. J. Microbiol.* 21, 1602–1607.
- Chen, X., Xiao, C., Chen, H.Y., 1987. Wufengian (Ashgillian) graptolite faunal differentiation and anoxic environment in South China. *Acta Palaeontol. Sin.* 26, 326–344.
- Chen, X., Rong, J., Li, Y., Boucot, A.J., 2004. Facies patterns and geography of the Yangtze region, South China, through the Ordovician and Silurian transition. *Palaeogeogr. Palaeoclimatol. Palaeoecol.* 204, 353–372.
- Chen, X., Fan, J.X., Wang, W.H., Wang, H.Y., Nie, H.K., Shi, X.W., Wen, Z.D., Chen, D.Y., Li, W.J., 2017. Stage-progressive distribution pattern of the Lungmachi black graptolitic shales from Guizhou to Chongqing, Central China. *Sci. China Earth Sci.* 60: 1133–1146. <http://dx.doi.org/10.1007/s11430-016-9031-9>.

- Compton, J.S., 1988. Degree of supersaturation and precipitation of organogenic dolomite. *Geology* 16, 318–321.
- Copper, P., 2001. Evolution, radiations, and extinctions in Proterozoic to Mid-Paleozoic reefs. In: Stanley, G.D.J. (Ed.), *The History and Sedimentology of Ancient Reef Systems*. Springer, pp. 89–119.
- Cuomo, M.C., Bartholomew, P.R., 1991. In: Tyson, R.V., Pearson, T.H. (Eds.), *Pelletal Black Shale Fabrics - Their Origin and Significance*. Geol Soc Spec Publ. Geological Society of London, pp. 221–232.
- Cuomo, M.C., Rhoads, D.C., 1987. Biogenic sedimentary fabrics associated with pioneering polychaete assemblages: modern and ancient. *J. Sediment. Res.* 57.
- Dashtgard, S.E., Snedden, J.W., MacEachern, J.A., 2015. Unbioturbated sediments on a muddy shelf: hypoxia or simply reduced oxygen saturation? *Palaeogeogr. Palaeoclimatol. Palaeoecol.* 425, 128–138.
- Delabroye, A., Vecoli, M., 2010. The end-Ordovician glaciation and the Hirnantian Stage: a global review and questions about Late Ordovician event stratigraphy. *Earth Sci. Rev.* 98, 269–282.
- Desrochers, A., Farley, C., Achab, A., 2010. A far-field record of the end Ordovician glaciation: the Ellis Bay Formation, Anticosti Island, Eastern Canada[J]. *Palaeogeogr. Palaeoclimatol. Palaeoecol.* 296 (3), 248–263.
- Diaz, R.J., Rosenberg, R., 1995. Marine benthic hypoxia: a review of its ecological effects and the behavioural responses of benthic macrofauna. *Oceanogr. Mar. Biol.* 33 (245–203).
- Ekdale, A.A., Mason, T.R., 1988. Characteristic trace-fossil associations in oxygen-poor sedimentary environments. *Geology* 16, 720–723.
- Fan, J., Peng, P., Melchin, M.J., 2009. Carbon isotopes and event stratigraphy near the Ordovician–Silurian boundary, Yichang, South China. *Palaeogeogr. Palaeoclimatol. Palaeoecol.* 276, 160–169.
- Fike, D.A., Bradley, A.S., Rose, C.V., 2015. Rethinking the ancient sulfur cycle. *Annu. Rev. Earth Planet. Sci.* 43, 593–622.
- Finlay, A.J., Selby, D., Gröcke, D.R., 2010. Tracking the Hirnantian glaciation using Os isotopes. *Earth Planet. Sci. Lett.* 293, 339–348.
- Fortey, R.A., Cocks, L.R.M., 2005. Late Ordovician global warming - the Boda event. *Geology* 33, 405–408.
- Gingras, M.K., MacEachern, J.A., Dashtgard, S.E., 2011. Process ichnology and the elucidation of physico-chemical stress. *Sediment. Geol.* 237, 115–134.
- Golonka, J., 2009. Phanerozoic Palaeoenvironment and Palaeolithofacies Maps: Early Paleozoic. 35. *Geologia/Akademia Górnicza-Hutnicza im. Stanisława Staszica w Krakowie*, pp. 589–654.
- Golonka, J., 2012. Paleozoic Palaeoenvironment and Palaeolithofacies Maps of Gondwana. AGH University of Science and Technology Press.
- Golonka, J., Krobicki, M., Pajak, J., Nguyen, V.G., Zuchiewicz, W., 2006. Global Plate Tectonics and Paleogeography of Southeast Asia. AGH University of Science and Technology, Arkadia, Krakow.
- Gorjan, P., Kaiho, K., Fike, D.A., Xu, C., 2012. Carbon- and sulfur-isotope geochemistry of the Hirnantian (Late Ordovician) Wangjiawan (riverside) section, South China: global correlation and environmental event interpretation. *Palaeogeogr. Palaeoclimatol. Palaeoecol.* 337–338, 14–22.
- Götte, J., Zimmerle, W., 2000. Quartz and Silica as Guide to Provenance in Sediments and Sedimentary Rocks.
- Habicht, K.S., Canfield, D.E., 1997. Sulfur isotope fractionation during bacterial sulfate reduction in organic-rich sediments. *Geochim. Cosmochim. Acta* 61, 5351–5361.
- Habicht, K.S., Canfield, D.E., 2001. Isotope fractionation by sulfate-reducing natural populations and the isotopic composition of sulfide in marine sediments. *Geology* 29, 555–558.
- Hallam, A., Wignall, P., 1999. Mass extinctions and sea-level changes. *Earth Sci. Rev.* 48, 217–250.
- Hoefs, J., 2008. *Stable Isotope Geochemistry*. Springer Science & Business Media.
- Holmden, C., Mitchell, C.E., LaPorte, D.F., 2013. Nd isotope records of late Ordovician sea-level change—Implications for glaciation frequency and global stratigraphic correlation[J]. *Palaeogeogr. Palaeoclimatol. Palaeoecol.* 386, 131–144.
- Ingvorsen, K., Jørgensen, B., 1984. Kinetics of sulfate uptake by freshwater and marine species of *Desulfovibrio*. *Arch. Microbiol.* 139, 61–66.
- Johnston, D.T., Macdonald, F.A., Gill, B.C., Hoffman, P.F., Schrag, D.P., 2012. Uncovering the Neoproterozoic carbon cycle. *Nature* 483, 320–323.
- Jones, D.S., Fike, D.A., 2013. Dynamic sulfur and carbon cycling through the end-Ordovician extinction revealed by paired sulfate–pyrite  $\delta^{34}\text{S}$ . *Earth Planet. Sci. Lett.* 363, 144–155.
- Jones, D.S., Fike, D.A., Finnegan, S., Fischer, W.W., Schrag, D.P., McCay, D., 2011. Terminal Ordovician carbon isotope stratigraphy and glacioeustatic sea-level change across Anticosti Island (Quebec, Canada). *Geol. Soc. Am. Bull.* 123, 1645–1664.
- Jones, D.S., Creel, R.C., Rios, B.A., 2016. Carbon isotope stratigraphy and correlation of depositional sequences in the Upper Ordovician Ely Springs Dolostone, eastern Great Basin, USA. *Palaeogeogr. Palaeoclimatol. Palaeoecol.* 458, 85–101.
- Kaljo, D., Hints, L., Hints, O., Männik, P., Martma, T., Nõlvak, J., 2011. Katian prelude to the Hirnantian (Late Ordovician) mass extinction: a Baltic perspective. *Geol. J.* 46, 464–477.
- Kaplan, I.R., Rittenberg, S.C., 1964. Microbiological fractionation of sulphur isotopes. *Microbiology* 34, 195–212.
- Kump, L.R., Arthur, M.A., Patzkowsky, M.E., Gibbs, M.T., Pinkus, D.S., Sheehan, P.M., 1999. A warming hypothesis for glaciation at high atmospheric  $\text{pCO}_2$  during the Late Ordovician. *Palaeogeogr. Palaeoclimatol. Palaeoecol.* 152, 173–187.
- LaPorte, D.F., Holmden, C., Patterson, W.P., Loxton, J.D., Melchin, M.J., Mitchell, C.E., Finney, S.C., Sheets, H.D., 2009. Local and global perspectives on carbon and nitrogen cycling during the Hirnantian glaciation. *Palaeogeogr. Palaeoclimatol. Palaeoecol.* 276, 182–195.
- Lazar, O.R., 2007. Redefinition of the New Albany Shale of the Illinois Basin: An Integrated, Stratigraphic, Sedimentologic, and Geochemical Study. ProQuest.
- Lazar, O.R., Bohacs, K.M., Schieber, J., 2015. Mudstone primer: Lithofacies variations, diagnostic criteria, and sedimentologic-stratigraphic implications at lamina to bedset scales[M]. SEPM Soc. Sediment. Geol.
- Leavitt, W.D., Halevy, I., Bradley, A.S., 2013. Influence of sulfate reduction rates on the Phanerozoic sulfur isotope record[J]. *Proc. Natl. Acad. Sci.* 110 (28), 11244–11249.
- Lefticariu, L., Pratt, L.M., Ripley, E.M., 2006. Mineralogical and sulfur isotopic effects accompanying oxidation of pyrite in millimolar solutions of hydrogen peroxide at temperatures from 4 to 150 °C. *Geochim. Cosmochim. Acta* 70, 4889–4905.
- Li, Y., Schieber, J., 2015. On the origin of a phosphate enriched interval in the Chattanooga Shale (Upper Devonian) of Tennessee—a combined sedimentologic, petrographic, and geochemical study. *Sediment. Geol.* 329, 40–61.
- Li, Z.-X., Li, X.-H., Wartho, J.-A., Clark, C., Li, W.-X., Zhang, C.-L., Bao, C., 2010. Magmatic and metamorphic events during the early Paleozoic Wuyi-Yunkai orogeny, southeastern South China: new age constraints and pressure-temperature conditions. *Geol. Soc. Am. Bull.* 122 (5–6), 772–793.
- Li, Y.F., Fan, T.L., Gao, Z.Q., Zhang, J.C., Wang, X.M., Zeng, W.T., Zhang, J.P., 2012. Sequence stratigraphy of silurian black shale and its distribution in the southeast area of Chongqing. *Nat. Gas Geosci.* 23, 299–306 (In Chinese).
- Li, Y., Fan, T., Zhang, J., Wei, X., Zhang, J., 2015a. Impact of paleoenvironment, organic paleoproductivity, and clastic dilution on the formation of organic-rich shales: a case study about the Ordovician-Silurian black shales, southeastern Chongqing, South China. *Arab. J. Geosci.* 1–15.
- Li, Y., Fan, T., Zhang, J., Zhang, J., Wei, X., Hu, X., Zeng, W., Fu, W., 2015b. Geochemical changes in the Early Cambrian interval of the Yangtze Platform, South China: implications for hydrothermal influences and paleocean redox conditions. *J. Asian Earth Sci.* 109, 100–123.
- Liang, C., Jiang, Z., Yang, Y., Wei, X., 2012. Characteristics of shale lithofacies and reservoir space of the Wufeng-Longmaxi Formation, Sichuan Basin. *Pet. Explor. Dev.* 39, 691–698.
- Liu, Y., Li, C., Algeo, T.J., Fan, J., Peng, P., 2016. Global and regional controls on marine redox changes across the Ordovician-Silurian boundary in South China. *Palaeogeogr. Palaeoclimatol. Palaeoecol.* 463, 180–191.
- Liu, Z., Algeo, T.J., Guo, X., Fan, J., Du, X., Lu, Y., 2017. Paleo-environmental cyclicity in the Early Silurian Yangtze Sea (South China): tectonic or glacio-eustatic control? *Palaeogeogr. Palaeoclimatol. Palaeoecol.* 466, 59–76.
- Loucks, R.G., Ruppel, S.C., 2007. Mississippian Barnett Shale: Lithofacies and depositional setting of a deep-water shale-gas succession in the Fort Worth Basin, Texas. *AAPG Bull.* 91, 579–601.
- MacEachern, J., Pemberton, S., Gingras, M., Bann, K., 2010. Ichnology and facies models. In: James, N.P., Dalrymple, R.W. (Eds.), *Facies Models 4*. Geological Association of Canada.
- Macquaker, J.H.S., Taylor, K.G., Gawthorpe, R.L., 2007. High-resolution facies analyses of mudstones: implications for paleoenvironmental and sequence stratigraphic interpretations of offshore ancient mud-dominated successions. *J. Sediment. Res.* 77, 324–339.
- Macquaker, J.H.S., Bentley, S.J., Bohacs, K.M., 2010. Wave-enhanced sediment-gravity flows and mud dispersal across continental shelves: reappraising sediment transport processes operating in ancient mudstone successions. *Geology* 38, 947–950.
- Marshall, J.D., Middleton, P.D., 1990. Changes in marine isotopic composition and the Late Ordovician glaciation. *J. Geol. Soc.* 147, 1–4.
- Marshall, J.D., Brencley, P.J., Mason, P., Wolff, G.A., Astini, R.A., Hints, L., Meidla, T., 1997. Global carbon isotopic events associated with mass extinction and glaciation in the late Ordovician. *Palaeogeogr. Palaeoclimatol. Palaeoecol.* 132, 195–210.
- Maynard, J.B., 1980. Sulfur isotopes of iron sulfides in Devonian-Mississippian shales of the Appalachian basin: control by rate of sedimentation. *Am. J. Sci.* 280 (8), 772–786.
- Melchin, M.J., Holmden, C., 2006. Carbon isotope chemostratigraphy in Arctic Canada: sea-level forcing of carbonate platform weathering and implications for Hirnantian global correlation. *Palaeogeogr. Palaeoclimatol. Palaeoecol.* 234, 186–200.
- Melchin, M.J., Mitchell, C.E., Holmden, C., Storch, P., 2013. Environmental changes in the Late Ordovician-early Silurian: review and new insights from black shales and nitrogen isotopes. *Geol. Soc. Am. Bull.* 125, 1635–1670.
- Melchin, M.J., Mitchell, C.E., 1991. Late Ordovician extinction in the Graptoloidea. *Advances in Ordovician geology. Geol. Surv. Can. Pap* 90, 59–78.
- Metcalfe, I., 1994. Late Paleozoic and Mesozoic paleogeography of eastern Pangea and Tethys. In: Embry, A.F., Beauchamp, B., Glass, D.J. (Eds.), *Pangea: Global Environments and Resources*. Canadian Society of Petroleum Geologists, pp. 97–111.
- Metcalfe, I., 2013. Gondwana dispersion and Asian accretion: tectonic and paleogeographic evolution of eastern Tethys. *J. Asian Earth Sci.* 66, 1–33.
- Migdisov, A.A., Ronov, A.B., Grinenko, V.A., 1983. The sulphur cycle in the lithosphere. In: Ivanov, M.V., Freney, J.R. (Eds.), *The global geochemical sulphur cycle*. John Wiley & Sons, New York, pp. 25–127.
- Mitchell, C.E., Storch, P., Holmden, C., Melchin, M.J., Gutiérrez-Marco, J.C., 2011. New stable isotope data and fossils from the Hirnantian Stage in Bohemia and Spain: implications for correlation and paleoclimate. In: Gutiérrez-Marco, J.C., Rábano, I., García-Bellido, D. (Eds.), *Ordovician of the World: Cuadernos del Museo Geominero. Instituto Geológico y Minero de España, Madrid, Spain*.
- Moreau, J., 2011. The late Ordovician deglaciation sequence of the sw Murzuq basin (Libya). *Basin Res.* 23, 449–477.
- Munnecke, A., Calner, M., Harper, D.A.T., Servais, T., 2010. Ordovician and Silurian seawater chemistry, sea level, and climate: a synopsis. *Palaeogeogr. Palaeoclimatol. Palaeoecol.* 296, 389–413.
- Pike, J., Bernhard, J.M., Moreton, S.G., Butler, I.B., 2001. Microbioturbation of marine sediments in dysoxic environments: implications for early sediment fabric formation and diagenetic processes. *Geology* 29, 923–926.

- Reaves, C.M., 1986. Organic matter metabolizability and calcium carbonate dissolution in nearshore marine muds. *J. Sediment. Res.* 56.
- Riese, D.J., 2014. The Significance of Crypto- and Macrobioturbation in the New Albany Shale for the Interpretation of Depositional Histories: An Integrated Approach Using Core Descriptions, CT Scans, Neochronology Experiments, and Geochemistry. Indiana University, ProQuest Dissertations Publishing.
- Rong, J.-Y., 1979. The Hirnantia fauna of China with comments on the Ordovician-Silurian boundary. *Acta Stratigr. Sin.* 3, 1–29.
- Rong, J.Y., 1984. Brachiopods of Latest Ordovician in the Yichang District, Western Hubei, Central China.
- Rong, J., Chen, X., 1987. Faunal differentiation, biofacies and lithofacies pattern of Late Ordovician (Ashgillian) in South China. *Acta Palaeontol. Sin.* 26, 507–535.
- Rong, J.Y., Chen, X., Harper, D.A., 2002. The latest Ordovician Hirnantia Fauna (Brachiopoda) in time and space. *Lethaia* 35, 231–249.
- Rong, J., Chen, X., Zhan, R., Fan, J., Wang, Y., Zhang, Y., Li, Y., Huang, B., Wu, R., Wang, G., 2010. New observation on Ordovician–Silurian boundary strata of southern Tongzi county, northern Guizhou, Southwest China. *J. Stratigr.* 34, 337–348.
- Rong, J., Chen, X., Wang, Y., Zhan, R., Liu, J., Huang, B., Tang, P., Wu, R., Wang, G., 2011. Northward expansion of Central Guizhou Oldland through the Ordovician and Silurian transition: evidence and implications. *Sci. China Earth Sci.* 41, 1407–1415.
- Savrdra, C.E., 2007. Trace fossils and marine benthic oxygenation. In: Miller, W. (Ed.), *Trace Fossils*. Elsevier, Amsterdam, pp. 149–158.
- Savrdra, C.E., Bottjer, D.J., 1991. Oxygen-related biofacies in marine strata: an overview and update. *Geol. Soc. Lond., Spec. Publ.* 58, 201–219.
- Schieber, J., 1990. Significance of styles of epicontinental shale sedimentation in the Belt Basin, Midproterozoic of Montana, USA. *Sediment. Geol.* 69, 297–312.
- Schieber, J., 1994. Evidence for high-energy events and shallow-water deposition in the Chattanooga Shale, Devonian, Central Tennessee, USA. *Sediment. Geol.* 93, 193–208.
- Schieber, J., 1996. Early diagenetic silica deposition in algal cysts and spores; a source of sand in black shales? *J. Sediment. Res.* 66, 175–183.
- Schieber, J., 1999. Distribution and deposition of mudstone facies in the Upper Devonian Sonyea Group of New York. *J. Sediment. Res.* 69, 909–925.
- Schieber, J., 2007. Oxidation of detrital pyrite as a cause for Marcasite Formation in marine lag deposits from the Devonian of the eastern US. *Deep-Sea Res. II Top. Stud. Oceanogr.* 54, 1312–1326.
- Schieber, J., 2011a. Marcasite in black shales—a mineral proxy for oxygenated bottom waters and intermittent oxidation of carbonaceous muds. *J. Sediment. Res.* 81, 447–458.
- Schieber, J., 2011b. Reverse engineering mother nature - shale sedimentology from an experimental perspective. *Sediment. Geol.* 238, 1–22.
- Schieber, J., 2011c. Shifting Paradigms in Shale Sedimentology—The Implications of Recent Flume Studies for Interpreting Shale Fabrics and Depositional Environments, Gas Shale of the Horn River Basin. Canadian Society of Petroleum Geologist Calgary, pp. 109–114.
- Schieber, J., 2016. Mud re-distribution in epicontinental basins – exploring likely processes. *Mar. Pet. Geol.* 71, 119–133.
- Schieber, J., Lazar, R., 2004. Devonian black shales of the eastern U.S.: new insights into sedimentology and stratigraphy from the subsurface and outcrops in the Illinois and Appalachian Basins. Field Guide for the 2004 Great Lakes Section SEPM Annual Field Conference.
- Schieber, J., Southard, J.B., 2009. Bedload transport of mud by floccule ripples—direct observation of ripple migration processes and their implications. *Geology* 37, 483–486.
- Schieber, J., Yawar, Z., 2009. A new twist on mud deposition—mud ripples in experiment and rock record. *The Sedimentary Record*. 7, pp. 4–8.
- Schieber, J., Krinsley, D., Riciputi, L., 2000. Diagenetic origin of quartz silt in mudstones and implications for silica cycling. *Nature* 406, 981–985.
- Schieber, J., Southard, J., Thaisen, K., 2007. Accretion of mudstone beds from migrating floccule ripples. *Science* 318, 1760–1763.
- Schieber, J., Lazar, R., Bohacs, K., 2010. Sedimentology and stratigraphy of shales: expression and correlation of depositional sequences in the Devonian of Tennessee, Kentucky and Indiana. AAPG 2010 Annual Convention in New Orleans.
- Schönlau, H.P., Ferretti, A., Gaggero, L., Hammarlund, E., Harper, D.A.T., Histon, K., Priewalder, H., Spötl, C., Štorch, P., 2011. The Late Ordovician glacial event in the Carnic Alps (Austria). In: Gutiérrez-Marco, J.C., Rábano, I., García-Bellido, D. (Eds.), *Ordovician of the World: Cuadernos del Museo Geominero*. Instituto Geológico y Minero de España, Madrid, Spain, pp. 515–526.
- Seal II, R.R., 2006. Sulfur isotope geochemistry of sulfide minerals. In: Vaughan, D.J. (Ed.), *Sulfide Mineralogy and Geochemistry*, pp. 633–677.
- Sim, M.S., Bosak, T., Ono, S., 2011. Large sulfur isotope fractionation does not require disproportionation. *Science* 333, 74–77.
- Stow, D., Huc, A.Y., Bertrand, P., 2001. Depositional processes of black shales in deep water. *Mar. Pet. Geol.* 18, 491–498.
- Su, W., Huff, W.D., Etensohn, F.R., Liu, X., Zhang, J.e., Li, Z., 2009. K-bentonite, black-shale and flysch successions at the Ordovician–Silurian transition, South China: possible sedimentary responses to the accretion of Cathaysia to the Yangtze Block and its implications for the evolution of Gondwana. *Gondwana Res.* 15, 111–130.
- Taylor, A., Goldring, R., 1993. Description and analysis of bioturbation and ichnofabric. *J. Geol. Soc.* 150, 141–148.
- Tyson, R., Pearson, T., 1991. Modern and ancient continental shelf anoxia: an overview. In: Tyson, R.V., Pearson, T.H. (Eds.), *Special Publications. Geol Soc Spec Publ.* Geological Society, London, pp. 1–24.
- Wang, K., Chatterton, B., Wang, Y., 1997. An organic carbon isotope record of Late Ordovician to early Silurian marine sedimentary rocks, Yangtze Sea, South China: implications for CO<sub>2</sub> changes during the Hirnantian glaciation. *Palaeogeogr. Palaeoclimatol. Palaeoecol.* 132, 147–158.
- Wang, X.-L., Shu, L.-S., Xing, G.-F., Zhou, J.-C., Tang, M., Shu, X.-J., Qi, L., Hu, Y.-H., 2012. Post-orogenic extension in the eastern part of the Jiangnan orogen: evidence from ca 800–760 Ma volcanic rocks. *Precambrian Res.* 222–223, 404–423.
- Wignall, P.B., 1991. Model for transgressive black shales? *Geology* 19, 167–170.
- Wilson, R.D., 2012. Facies analysis and sequence stratigraphy of the Middle Devonian (Givetian) Genesee Formation of New York. Implications for Accommodation During a Eustatic Sea-level Rise. Indiana University.
- Wu, M., 2016. The Study on Black Shale Microfacies of Upper Ordovician and Lower Silurian in South Sichuan Basin. China University of Geosciences (Beijing), Beijing.
- Yan, D., Chen, D., Wang, Q., Wang, J., Wang, Z., 2009. Carbon and sulfur isotopic anomalies across the Ordovician–Silurian boundary on the Yangtze Platform, South China. *Palaeogeogr. Palaeoclimatol. Palaeoecol.* 274, 32–39.
- Yan, D., Chen, D., Wang, Q., Wang, J., 2010. Large-scale climatic fluctuations in the latest Ordovician on the Yangtze block, south China. *Geology* 38, 599–602.
- Yan, D., Chen, D., Wang, Q., Wang, J., 2012. Predominance of stratified anoxic Yangtze Sea interrupted by short-term oxygenation during the Ordo-Silurian transition. *Chem. Geol.* 291, 69–78.
- Yao, J., Shu, L., Santosh, M., Li, J., 2013. Geochronology and Hf isotope of detrital zircons from Precambrian sequences in the eastern Jiangnan Orogen: constraining the assembly of Yangtze and Cathaysia Blocks in South China. *J. Asian Earth Sci.* 74, 225–243.
- Zhang, L., Fan, J., Chen, Q., 2014. Reconstruction of the mid-Hirnantian palaeotopography in the Upper Yangtze region, South China[J]. *Est. J. Earth Sci.* 63 (4), 329.
- Zhang, L.N., Fan, J.X., Chen, Q., 2016. Geographic distribution and palaeogeographic reconstruction of the Upper Ordovician Kuanyinchiao Bed in South China (in Chinese). *Chin. Sci. Bull.* 61:2053–2063. <http://dx.doi.org/10.1360/N972015-00981>.
- Zhang, T., Kershaw, S., Wan, Y., Lan, G., 2000. Geochemical and facies evidence for palaeoenvironmental change during the Late Ordovician Hirnantian glaciation in South Sichuan Province, China. *Glob. Planet. Chang.* 24, 133–152.
- Zhang, T., Shen, Y., Zhan, R., Shen, S., Chen, X., 2009. Large perturbations of the carbon and sulfur cycle associated with the Late Ordovician mass extinction in South China. *Geology* 37, 299–302.
- Zheng, H., Gao, B., Peng, Y., Nie, H., Yang, F., 2013. Sedimentary evolution and shale gas exploration direction of the Lower Silurian in Middle-Upper Yangtze area. *J. Palaeogeogr.* 15, 645–656.
- Zhou, L., Algeo, T.J., Shen, J., Hu, Z., Gong, H., Xie, S., Huang, J., Gao, S., 2015. Changes in marine productivity and redox conditions during the Late Ordovician Hirnantian glaciation. *Palaeogeogr. Palaeoclimatol. Palaeoecol.* 420, 223–234.
- Zinkernagel, U., 1978. Cathodoluminescence of quartz and its application to sandstone petrology.